The endoplasmic reticulum in perisynaptic astrocytic processes: shape, distribution and effect on calcium activity

Audrey Denizot [1*], María Fernanda Veloz Castillo [2], Pavel Puchenkov [3], Corrado Calì [4,5], Erik De Schutter [1]

[1] Okinawa Institute of Science and Technology, Computational Neuroscience Unit, Onna-Son, Japan

[2] Biological and Environmental Science and Engineering Division, King Abdullah University of Science and Technology, Thuwal, Saudi Arabia

[3] Okinawa Institute of Science and Technology, Scientific Computing and Data Analysis section, Research Support Division, Onna-Son, Japan

[4] Department of Neuroscience, University of Torino, Italy

[5] Neuroscience Institute Cavalieri Ottolenghi, Orbassano, Italy

[*]To whom correspondence should be addressed; E-mail: audrey.denizot3@oist.jp.

Astrocytes recently emerged as key regulators of information processing in the brain. Ca^{2+} signals in perisynaptic astrocytic processes (PAPs) notably allow astrocytes to fine-tune neurotransmission at so-called tripartite synapses. As most PAPs are below the diffraction limit, their content in Ca^{2+} stores and the contribution of the latter to astrocytic Ca^{2+} activity is unclear. Here, we reconstruct tripartite synapses in 3D from electron microscopy and find that 75% of PAPs contain some endoplasmic reticulum (ER), a major astrocytic Ca^{2+} store, displaying strikingly diverse geometrical properties. To investigate the role of such spatial properties, we implemented an algorithm that creates 3D PAP meshes of various ER distributions and constant shape. Reaction-diffusion simulations in those meshes reveal that astrocyte activity is shaped by a complex interplay between the location of Ca^{2+} channels, Ca^{2+} buffering, ER shape and distribution. Overall, this study sheds new light into mechanisms regulating signal transmission in the brain.

Introduction

Astrocytes, the most abundant glial cells of the central nervous system, are essential to numerous brain functions [74]. Notably, astrocytes are key modulators of neurotransmission at so-called tripartite synapses [4, 60]. A single astrocyte in the CA1 region of the mouse hippocampus is in contact with hundreds of thousands of synapses simultaneously, at perisynaptic astrocytic processes (PAPs) [14]. Around 75 % of cortical and 65 % of hippocampal synapses are contacted by an astrocytic process [78, 46]. This close contact between astrocytes and neurons allows astrocytes to control various synaptic functions, from glutamate uptake [37], and spillover [34, 9], to synapse homeostasis [57], stability [11], synaptogenesis [73], and neurotransmission [3, 60]. Those synaptic functions are associated with specific local molecular expression in PAPs [49, 28], which changes upon fear conditioning [49]. Importantly, the alteration of the proximity of PAPs to hippocampal synapses of the CA1 region *in vivo* affects neuronal activity and cognitive performance [9]. Conversely, neuronal activity has been shown to induce the remodeling of synaptic coverage by PAPs in various brain regions, both *in vivo* and in acute slices [34, 51, 54, 11, 46, 56, 29, 76]. Together, those results illustrate that PAPs are preferential sites of neuron-astrocyte communication. Although the recent emergence of super-resolution techniques has provided key insights into the properties and functions of PAPs [33, 5], our understanding of PAP physiology and function in live tissue is hindered by their nanoscopic size [59, 1].

Ca^{2+} signals are commonly interpreted as a measure of astrocyte activity, notably in response to neurotransmitter release at synapses [75, 59, 61]. The recent advances in Ca^{2+} imaging approaches have improved the spatio-temporal resolution of Ca^{2+} signals in astrocytes [64, 61]. Strikingly, it revealed that astrocytes in acute slices and *in vivo* exhibit spatially-restricted Ca^{2+} signals, also referred to as hotspots or microdomains, stable over time and which activity varies under physiological conditions such as locomotion or sensory stimulation [44, 30, 2, 12, 8, 66, 70, 69, 68, 63, 53, 25, 45]. Growing evidence supports that PAPs are preferential sites displaying spatially-restricted Ca^{2+} microdomains in response to neurotransmission [53, 25, 52, 7, 44]. As a single astrocyte can contact hundreds of thousands of synapses simultaneously [14], such spatially-restricted Ca^{2+} microdomains might enable the astrocyte to finely tune synaptic transmission at the single synapse level.

mGluR activation on the astrocytic membrane following neurotransmission at glutamatergic synapses results in Ca^{2+} transients mediated by G_q proteins and Ca^{2+} stores such as the endoplasmic reticulum (ER) [64], which can trigger the release of molecules that modulate neurotransmission, referred to as gliotransmitters[15, 48, 3, 60]. Most astrocytic Ca^{2+} signals are mediated by the Inositol 3-Phosphate (IP_3) receptors on the membrane of the endoplasmic reticulum (ER) [62]. Because of their nanoscopic size, the Ca^{2+} pathways involved in microdomain Ca^{2+} signals in PAPs are still unclear. Notably, the presence of ER in PAPs and its involvement in microdomain Ca^{2+} signals at synapses is highly debated. During the last decade, PAPs have

2

notably been regarded as devoid of ER, with a minimum distance between the synapse and the closest astrocytic ER $> 0.5 \ \mu m$ [55, 59]. In contrast, inhibiting ER-mediated Ca^{2+} signaling in fine processes results in a decreased number of Ca^{2+} domains [2] and a decreased Ca^{2+} peak frequency [2, 7, 63]. Furthermore, some astrocytic ER has been detected near synapses in other EM studies [1, 10]. Yet, the geometrical properties of the ER in PAPs and its distribution remain poorly characterized, but could have a strong impact on neuron-astrocyte communication at tripartite synapses.

Here, we use a 220 μm^3 hippocampal astrocytic volume from the CA1 stratum radiatum region (6 nm voxel resolution) [17], reconstructed from electron microscopy (EM), to create 46 three dimensional meshes of tripartite synapses. Strikingly, we find that 75 % of PAPs contain some ER, which can be as close as 72 nm to the post-synaptic density (PSD). Analysis of the geometrical features of those meshes reveal the vast diversity of ER shapes and distributions within PAPs from a single cell. We then used a detailed stochastic reaction-diffusion model of Ca^{2+} signals in PAPs to investigate the mechanistic link between the spatial features of the ER measured in the 3D meshes and the spatio-temporal properties of Ca^{2+} microdomain activity in PAPs. To be able to decipher the effect of ER distribution within the PAP independently from the effect of its shape, we developed an algorithm that automatically creates realistic 3D tetrahedral PAP meshes with various ER distributions from the realistic meshes reconstructed from EM. *In silico* experiments in those meshes reveal that the spatio-temporal properties of Ca^{2+} signals in PAPs are tightly regulated by a complex interplay between the clustering of Ca^{2+} channels, the ratio between ER surface area and PAP volume, Ca^{2+} buffering and ER spatial distribution. Together, this study provides new insights into the geometrical properties of hippocampal tripartite synapses and predicts mechanistic links between those features and Ca^{2+} microdomain activity at tripartite synapses.

Results

Quantification of the main geometrical properties of hippocampal tripartite synapses

To characterize the presence, shape and distribution of the endoplasmic reticulum (ER) in perisynaptic astrocytic processes (PAPs), we used a 220 μm^3 (7.07 μm x 6.75 μm x 4.75 μm) hippocampal astrocytic volume from the CA1 stratum radiatum region reconstructed from a perfectly isotropic EM stack (6 nm voxel resolution) [17]. Elements from the neuropil, i.e. boutons, dendritic spines and post-synaptic densities (PSDs), were also reconstructed. Following the workflow presented in Fig. 1A, forty four excitatory and two inhibitory tripartite synapse meshes were created, containing all elements belonging to the astrocyte and to the neuropil within a cube of 1.5 μm edge length (3.375 μm^3) centered at the center of mass of the PSD (Supplementary Movie 1). Five of those tripartite synapse meshes are displayed in Fig. 1B.

3
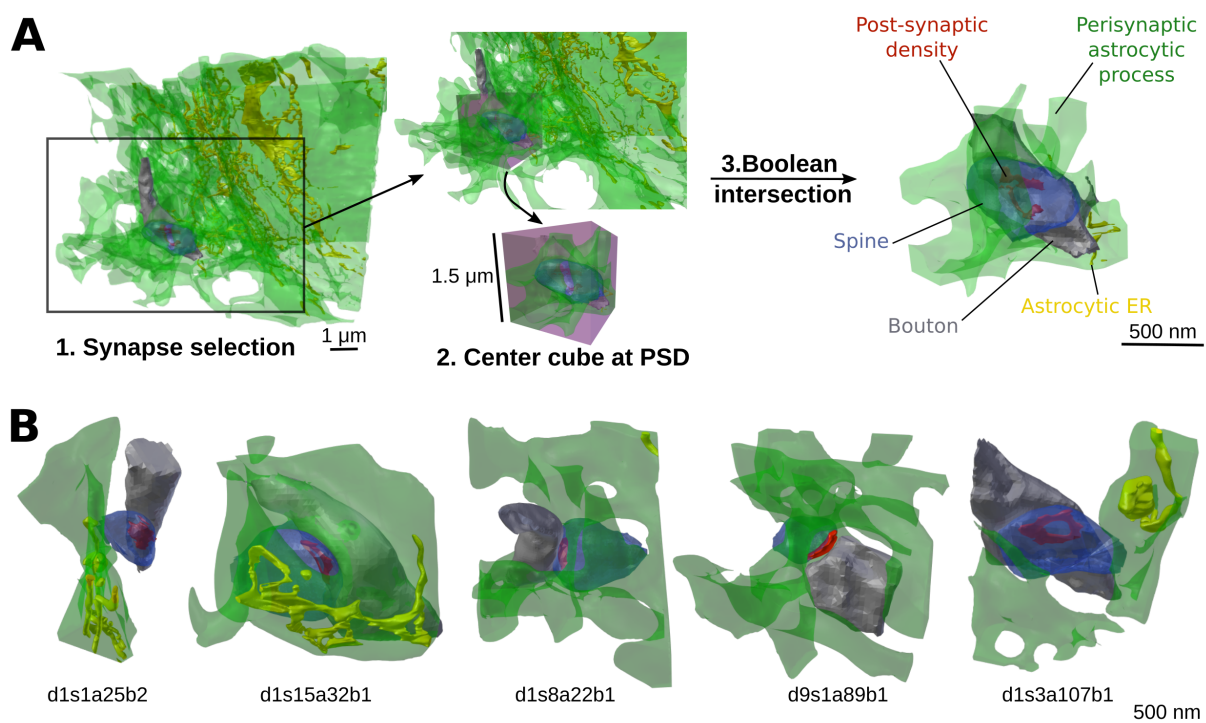
Fig 1: **Reconstruction of 46 tripartite synapse meshes from electron microscopy.** (A) Schematic presenting our tripartite synapse mesh creation workflow, here performed on synapse d10s1a2b1. 1. Synapses in contact with the 220 μm^3 astrocytic volume were selected one by one. 2. A cube of 1.5 μm edge length (3.375 μm^3) was created and centered at the center of mass of the post-synaptic density (PSD, red). 3. Boolean intersection between the neuronal and astrocytic objects and the cube resulted in the isolation of the elements of the tripartite synapse mesh: the perisynaptic astrocytic process (PAP, green), the astrocytic endoplasmic reticulum (ER, yellow), the bouton (grey) and the spine (blue). This workflow resulted in the creation of 44 excitatory and 2 inhibitory tripartite synapse meshes. (B) Images of five of the 3D tripartite synapse meshes created, d1s1a25b2, d1s15a32b1, d1s8a22b1, d9s1a89b1, d1s3a107b1, revealing their diverse geometrical properties.

4

Among those meshes, seventeen were located at the borders of the 220 μm^3 astrocytic volume. They were thus omitted from data analysis as synaptic elements in those meshes could not be fully reconstructed. The volume, surface area and surface-volume ratio (SVR) of each synaptic element, i.e the PAP, astrocytic ER, spine and bouton, of the remaining twenty seven fully reconstructed excitatory tripartite synapses are presented in Fig. 2C-E and Supplementary Table S1. The minimum distance between each vertex on the membrane of the PAP and the center of mass of the PSD was measured in each of the twenty seven meshes (Fig. 2B), providing a quantification of the distribution of the astrocyte around the synapse. Our results highlight the diverse distances between PSDs and PAPs belonging to a single cell. In accordance with previous studies [46, 50, 55], PAP membrane vertices could be as close as 5 nm to the PSD, with an average distance between the PSD and the closest PAP vertex of 65 nm. Importantly, we found that PM-PSD distance is the shortest, i.e PAPs are the closest to the synapse, when bouton surface area is low (Fig. 2F, p=0.013). PAP-PSD distance was not correlated to the surface area of the PAP (Fig. 2G, p=0.14) or spine (Fig. 2H, p=0.24).

Presence and geometrical properties of the endoplasmic reticulum in perisynaptic astrocytic processes

Because of the small size of most PAPs, the Ca^{2+} pathways that regulate astrocytic Ca^{2+} microdomain activity at tripartite synapses remain to be uncovered. Notably, the presence of ER in PAPs is controversial [55, 1, 10, 41]. We have thus analyzed the presence and shape of the ER in the PAPs from the twenty seven fully reconstructed excitatory tripartite synapse meshes presented in Fig. 2.

75% of PAPs contained some ER (Fig. 3C), which challenges the widespread belief that tripartite synapses are devoid of astrocytic ER. ER surface area, volume and SVR were measured in ER-containing PAPs and highlight that ER shape is highly variable between PAPs from the same cell (Fig. 3B). Note that there was no significant difference between bouton, spine and PAP surface area, volume and SVR between synapses with vs without astrocytic ER (Supplementary Fig. S1). We further characterized the vicinity of the astrocytic ER to the synapse. To do so, we measured the distance between each vertex on the ER membrane to the center of mass of the PSD (n=20). We found that ER-PSD distance varies drastically from synapse to synapse (Fig. 3E) and can be as little as 72 nm, far below the > 0.5 μm ER-PSD distance reported previously [55, 59]. The closest ER vertex was on average 432 nm away from the center of mass of the PSD. Interestingly, the larger the surface area of the ER, the closer it was to the PSD (Fig. 3F, p=0.013). Astrocytic ER was closer to the PSD in PAPs with higher surface area (Fig. 3G, p=0.024). The minimum ER-PSD distance was not correlated to the surface area of the spine (Fig. 3H, p=0.54) or bouton (Fig. 3I, p=0.29). Overall, our results highlight that most PAPs contain some ER and that its shape is highly variable, which could have strong implications on ER-dependent Ca^{2+} signaling in PAPs resulting from synaptic transmission.

5
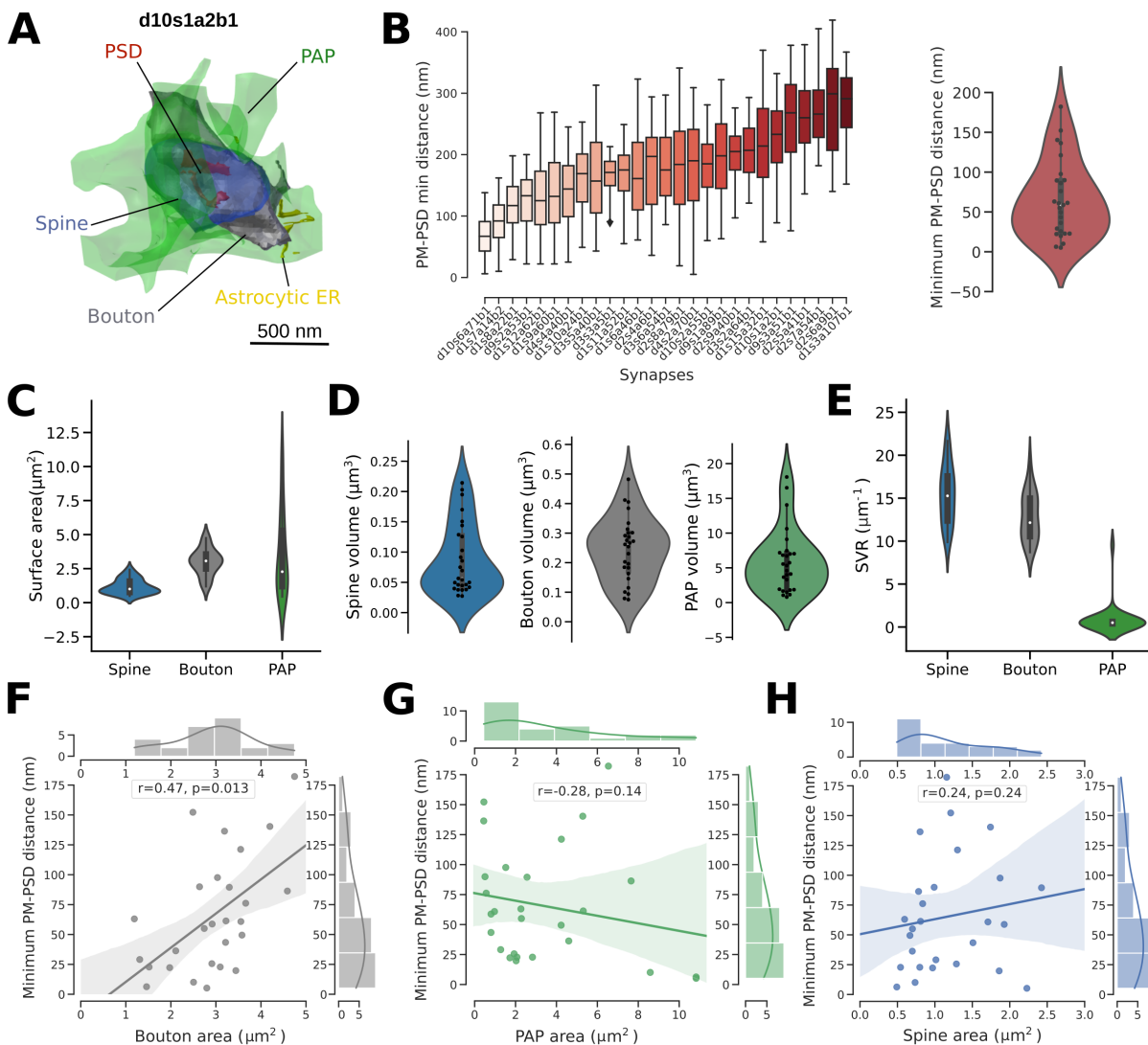
Fig 2: **Characterization of the geometrical properties of hippocampal tripartite synapses.**
(A) Image of a tripartite synapse mesh, d10s1a2b1, containing a bouton (grey), spine (blue), post-synaptic density (PSD, red), perisynaptic astrocytic process (PAP, green) and the astrocytic endoplasmic reticulum (ER, yellow). (B) Left: Boxplots presenting the distribution of the minimum distance between each vertex on the PAP membrane and the center of mass of the PSD, measured in the twenty seven excitatory tripartite synapse meshes fully reconstructed in this study. Right: Distribution of the minimum distance between the PAP and the PSD (n=27). (C-E) Violin plots presenting the distribution of spine, bouton and PAP surface area (C), volume (D) and surface-volume ratio (E). (F-H) Scatterplots presenting the variation of the minimum PAP-PSD distance as a function of bouton surface area (left), PAP surface area (middle) and spine surface area (right). Plots are presented with univariate kernel density estimation curves and a linear regression fit. Spearman correlation coefficients, r, and p-values, p, are displayed onto each regression plot, n=27.
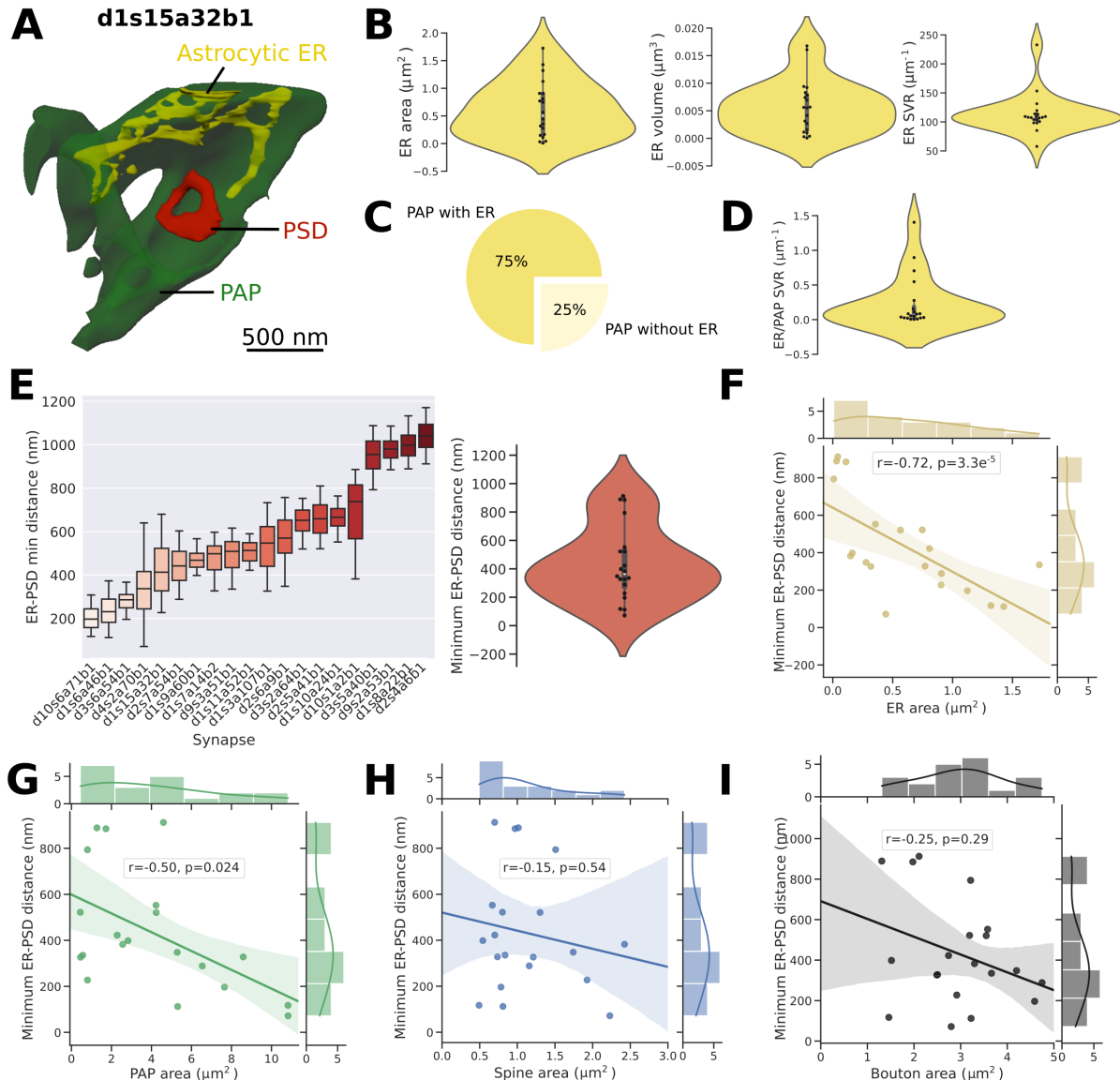
Fig 3: **Presence and geometrical properties of the endoplasmic reticulum in perisynaptic astrocytic processes.** (A) Image of the d1s15a32b1 PSD (red) and the neighboring PAP (green), that contains ER (yellow). (B) Violin plots representing the distribution of ER surface area (left), volume (middle) and surface volume ratio (right) within PAPs, n=20. (C) Among the twenty seven fully reconstructed PAP meshes extracted, 75 % contained some ER. (D) Distribution of the ratio between the ER surface area and PAP volume (n=20). (E) Quantitative analysis of the distance between the astrocytic ER and the neighboring PSD, n=20. (Left) Boxplots presenting the distribution of the distance of ER membrane vertices to the center of mass of the PSD in each PAP. (Right) Distribution of the minimum ER-PSD distance in PAPs, n=20. The lowest ER-PSD distance measured was 70nm (synapse d4s2a70b1).

Fig 3: (F-I) Scatterplots presenting the variation of the minimum ER-PSD distance as a function of ER surface area (F), PAP surface area (G), spine surface area (H) and bouton surface area (I), n=20. Plots are presented with univariate kernel density estimation curves and a linear regression fit. Spearman correlation coefficient, r, and p-value, p, are displayed onto each regression plot.

Reaction-diffusion simulations reveal different spatio-temporal properties of Ca^{2+} signals in PAPs of the same cell

PAPs are characterized by highly diverse sizes and shapes of the ER (Fig. 3), which could have strong implications on ER-mediated Ca^{2+} signals in PAPs. Because of their nanometric size, measuring Ca^{2+} activity and deciphering the involvement of ER-mediated signals in individual PAPs in live tissue is extremely challenging [61]. A better understanding of the mechanistic link between the geometrical properties of the ER and the spatio-temporal properties of Ca^{2+} microdomain signals in PAPs is crucial, yet hard to test experimentally. Here, we use the PAP meshes presented in Fig. 3 together with a spatial stochastic model of Ca^{2+} signaling adapted from the model of Denizot and collaborators [20] to investigate the mechanistic link between ER shape and Ca^{2+} microdomain activity in PAPs. Ca^{2+} influx in the PAP cytosol in the model is mediated by Inositol 3-Phosphate (IP_3) receptors on the membrane of the ER and by Ca^{2+} channels at the plasma membrane, Ch_{PM}. The reactions modeled are presented in Fig. 4A and in the Methods section. Neuronal activity was simulated at t=1s by infusing 50 IP_3 molecules at the PM of the PAP. The implementation of this model with STEPS software [35] allows to perform simulations in tetrahedral meshes in 3 spatial dimensions, such as the ones created in this study. Representative Ca-GCaMP traces in a cylindrical mesh, corresponding to the concentration of Ca^{2+} bound to Ca^{2+} indicators added to the cytosol of the model, display similar spatio-temporal characteristics to Ca^{2+} signals measured in organotypic hippocampal astrocytic cultures [21] (Fig. 4A, right).

We performed simulations in six PAP meshes reconstructed from electron microscopy, characterized by various geometrical properties of the ER: d1s3a107b1, d1s8a22b1, d1s10a24b1, d2s6a9b1, d9s4a34b1 and d10s1a2b1 (Fig. 4B, Table 1). To do so, meshes were pre-processed to allow their use in reaction-diffusion simulations. The pre-processing workflow is described in Fig. 4C and in the Methods section, and produced 3D tetrahedral meshes from the 2D triangular meshes reconstructed from EM. Screenshots of simulations performed in two realistic tetrahedral PAP meshes are presented in Fig. 4B. Ca-GCaMP and free Ca^{2+} signals, in simulations with and without Ca^{2+} indicators in the cytosol, respectively, were measured in d1s3a107b1, d1s8a22b1, d1s10a24b1, d2s6a9b1, d9s4a34b1 and d10s1a2b1 PAP meshes. A simulation in PAP d9s4a34b1 is presented in Supplementary movie 2. Representative traces are displayed in Fig. 4E. Signals varied greatly depending on the mesh (Fig. 4F). Note that, in accordance with previous studies [20, 81], Ca-GCaMP and free Ca^{2+} signals displayed different spatio-

Table 1: **Characteristics of the 3D PAP meshes used in the reaction-diffusion simulations.** V_{cyt} is the cytosolic volume, S_{PM} is the plasma membrane surface area, S_{ER} is the ER surface area, $SVR_{ER/PAP}$ is the ratio between the ER surface area and the cytosolic volume. ER_c is the number of ER vertices at ER-PM contact sites, i.e ≤ 20 nm from the closest PM vertex. d1s15a32b1$_{f0}$, d1s15a32b1$_{f21}$, d1s15a32b1$_{f64}$ and d1s15a32b1$_{f250}$ refer to meshes from frames 0, 21, 64 and 250 of the d1s15a32b1 PAP mesh presented in Fig. 8-9.

Geom	V_{cyt} (μm^3)	S_{PM} (μm^2)	S_{ER} (μm^2)	$SVR_{ER/PAP}$ (μm^{-1})	ER_c
$d1s3a107b1$	0.112	2.00	0.315	2.81	183
$d1s8a22b1$	0.397	8.60	0.031	0.078	31
$d1s10a24b1$	0.331	5.80	0.344	1.04	0
$d2s6a9b1$	0.505	10.0	0.273	0.54	158
$d9s4a34b1$	0.410	7.05	0.807	1.97	20958
$d10s1a2b1$	0.531	10.0	0.136	0.26	3771
d1s15a32b1$_{f0}$	0.426	6.91	0.85	2.00	295
d1s15a32b1$_{f21}$	0.426	6.91	0.85	2.00	2337
d1s15a32b1$_{f64}$	0.426	6.91	0.85	2.00	1683
d1s15a32b1$_{f250}$	0.426	6.91	0.85	2.00	2408
PAP1$_v$	0.434	3.55	0.088	0.21	0
PAP1$_w$	0.432	3.55	0.428	0.99	0
PAP1$_x$	0.428	3.55	0.834	1.95	125
PAP1$_y$	0.423	3.55	1.27	3.00	0
PAP1$_z$	0.418	3.55	1.62	3.88	555

163 temporal properties (Fig. 4F). Those results suggest that the diverse geometrical features of
164 PAPs and ER reported in this study (Fig. 2-3) strongly influence Ca^{2+} microdomain activity at
165 tripartite synapses.

The effect of IP3R clustering differs from PAP to PAP

167 IP$_3$R channels are not randomly distributed on the surface of the ER and form stable clusters of
168 various sizes [77, 72, 71, 67]. Numerous computational studies performed in 2 spatial dimen-
169 sions have predicted that IP$_3$R cluster size shapes Ca^{2+} activity (see [58] for a review). Whether
170 this effect still holds in 3D, notably in complex shapes such as that of the PAPs reconstructed
171 in this study, remains to be uncovered. We thus next simulated Ca^{2+} signaling in the 6 realistic
172 PAP meshes presented in Fig. 4, reconstructed from EM, d1s3a197b1, d1s8a22b1, d1s10a24b1,
173 d2s6a9b1, d9s4a34b1 and d10s1a2b1, with various distributions of IP$_3$Rs on the membrane of
174 the ER.
175 Simulations of the model were performed with different IP$_3$R cluster sizes η. Ca^{2+} chan-
176 nels were either randomly placed on the membrane of the PAP (cocl=0) or clustered onto the
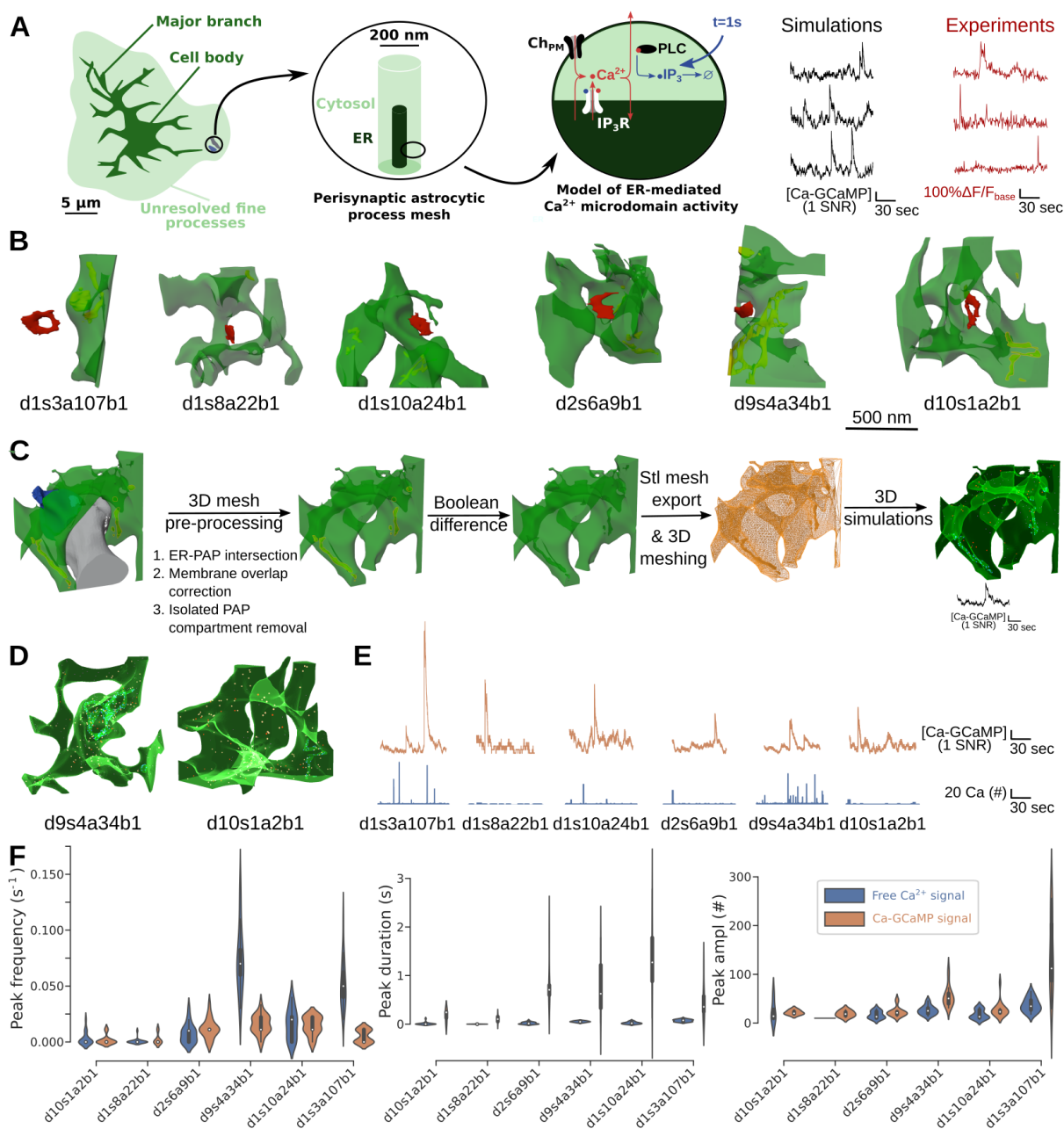
Fig 4: **Reaction-diffusion simulations reveal different spatio-temporal properties of** Ca^{2+} **signals between PAPs of the same cell.** (Left) Schematic representation of the model of Ca^{2+} signaling in PAPs used in this study. The model is stochastic, spatially-extended and simulations can be performed in 3D meshes. Ca^{2+} influx into the cytosol results from Ca^{2+} channels on the plasma membrane and from IP_3R channels on the ER. At t=1s, 50 IP_3 molecules were injected at the plasma membrane of the PAP, simulating neuronal activity. (Right) Representative Ca-GCaMP traces from simulations in a cylindrical mesh, 200 nm in diameter, 1 μm long (left, black) and experiments (right, red) [21].

Fig 4: (B) Images representing the 6 PAP meshes in which simulations were performed: d1s3a197b1, d1s8a22b1, d1s10a24b1, d2s6a9b1, d9s4a34b1 and d10s1a2b1. (C) Workflow to prepare the PAP meshes for 3D simulations illustrated on d2s6a9b1 mesh (see Methods section). The geometrical features of the resulting PAP meshes are presented in Table 1. (D) Screenshots of simulations in PAP meshes d9s4a34b1 and d10s1a2b1. Note that the darker and lighter greens result from 3D shading and rendering of the meshes. (E) Representative Ca-GCaMP (top, orange) and free Ca^{2+} (bottom, blue). Ca^{2+} traces were measured in separate simulations, where no GCaMP was added into the cytosol of the PAP. IP_3R channels and Ca^{2+} channels at the plasma membrane, Ch_{PM}, were randomly distributed onto the ER membrane and plasma membrane, respectively. (F) Quantification of peak frequency (left), duration (middle) and amplitude (right) of free Ca^{2+} (left, blue, n=20) and Ca-GCaMP (right, orange, n=20) signals measured *in silico* in 3D meshes of the PAPs presented in panel B.

177   PM triangles that were the closest to the ER triangles containing an IP_3R cluster (cocl=1), em-
178   ulating co-localization of Ca^{2+} channels, reported in neurons and astrocytes [43]. As IP_3R
179   density was kept constant across simulations, $3.5e^{-3}/\mu m^2$ [20], the total number of IP_3Rs,
180   N_{IP3R}, varied depending on the mesh: 90, 230, 78, 8, 40 and 96 in PAP meshes from synapses
181   d1s3a107b1, d9s4a34b1, d2s6a9b1, d1s8a22b1, d10s1a2b1 and d1s10a24b1, respectively. As
182   IP_3R cluster size was a divider of N_{IP3R}, cluster sizes tested varied slightly depending on the
183   mesh. The range of IP_3R cluster size tested varied from η=1-26. Representative free Ca^{2+}
184   traces measured in d1s3a197b1, d1s8a22b1, d1s10a24b1, d2s6a9b1, d9s4a34b1 and d10s1a2b1
185   PAP meshes with various IP_3R cluster sizes η are displayed in Fig. 5B. Strikingly, IP_3R cluster-
186   ing only affected Ca^{2+} activity in a subset of the PAP meshes studied (Fig. 5C). Indeed, Ca^{2+}
187   peak duration and amplitude increased with IP_3R cluster size in PAP meshes from synapses
188   d1s3a107b1 (ANOVA, p=$5.1e^{-5}$ and $1.9e^{-7}$), d2s6a9b1 (ANOVA, p=$3.16e^{-3}$ and 0.026) and
189   d9s4a34b1 (ANOVA, p=0.018 and 0.028) but not in d1s10a24b1 (ANOVA, p=0.44 and 0.32)
190   and d10s1a2b1 (ANOVA, p=0.69 and 0.83). This effect was associated with an increased fre-
191   quency of IP_3R opening with cluster size in d1s3a107b1, d2s6a9b1 and d9s4a34b1 meshes
192   (ANOVA, p=$3.4e^{-4}$, 0.007 and 0.037, respectively). Conversely, cluster size had no effect on
193   IP_3R opening frequency in d1s10a24b1 (ANOVA, p=0.050) and d10s1a2b1 (ANOVA, p=0.15).
194   Interestingly, such differences in IP_3R clustering effects on Ca^{2+} activity were still observed
195   in the absence of co-localization of Ca^{2+} channels at the plasma membrane with IP_3R clusters
196   (Supplementary Fig. S2). Those results highlight that different PAP and ER shapes are associ-
197   ated with different IP_3R clustering effects.
198
199   Interestingly, increased neuronal stimulation, simulated as an increased amount of IP_3 in-
200   fused, i, in the PAP at t=1s, triggered clustering effects in a PAP in which no clustering effect
201   was observed after a milder neuronal stimulation (Fig. 5D). This effect was characterized by an
202   increase of Ca^{2+} peak amplitude (ANOVA, p= $8.2e^{-5}$ for i=150 and p=$4.66e^{-7}$ for i=200), fre-
203   quency (ANOVA, p=0.005 for i=150 and p=0.006 for i=200) and duration (ANOVA, p=$3.4e^{-5}$
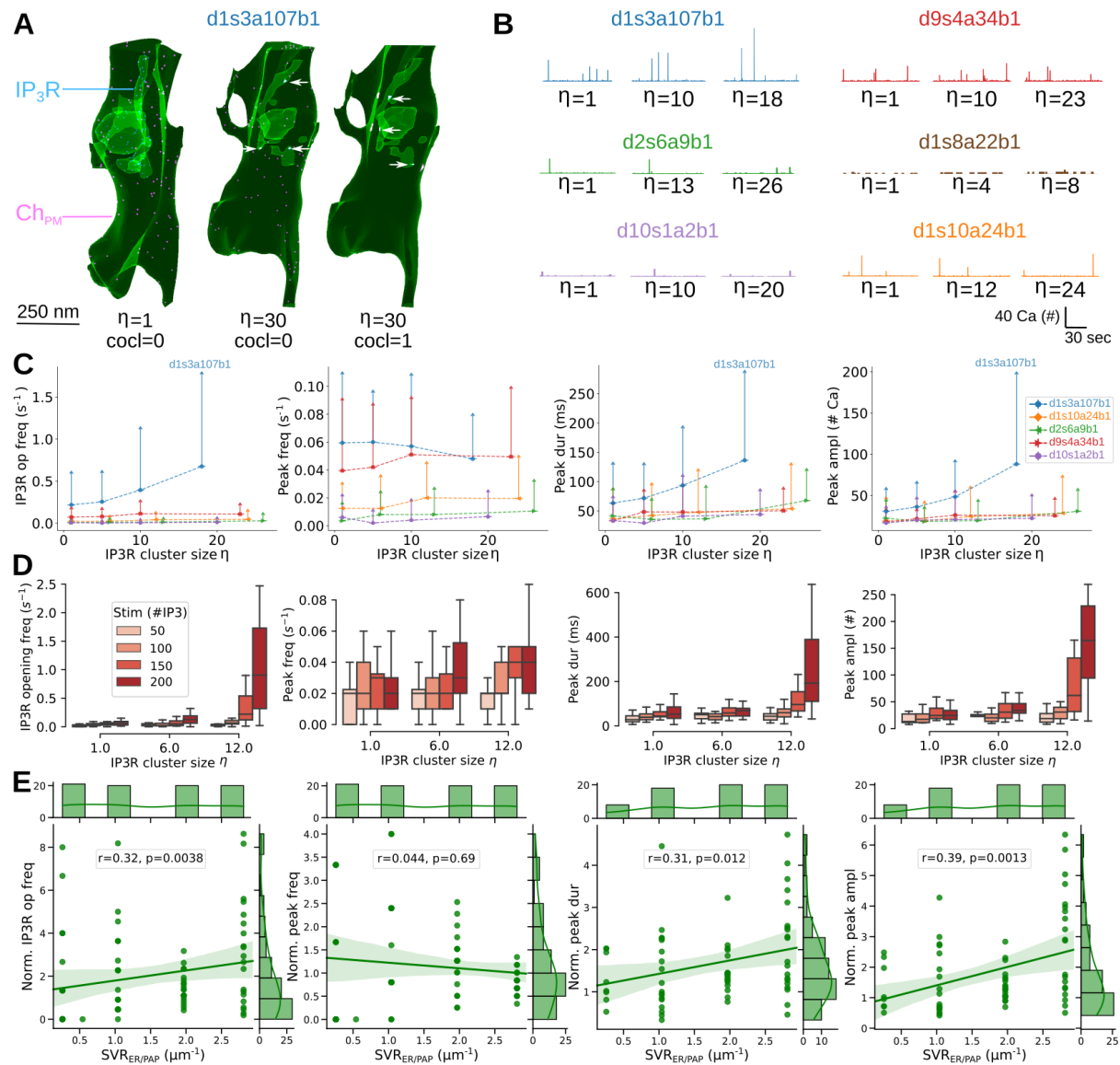
Fig 5: **The effect of IP_3R clustering differs from PAP to PAP.** (A) Screenshots of simulations in d1s3a107b1, with IP_3R cluster size η=1 and η=30. Simulations were performed with (cocl=1) and without (cocl=0) co-clustering of Ca^{2+} channels at the plasma membrane (purple) with IP_3Rs on the ER (blue). IP_3R clusters are indicated with a white arrow. (B) Representative free Ca^{2+} traces measured *in silico* in d1s3a107b1 (blue), d9s4a34b1 (red), d2s6a9b1 (green), d1s8a22b1 (brown), d10s1a2b1 (purple) and d1s10a24b1 (orange) meshes. (*C*) Quantification of IP_3R opening frequency (left), Ca^{2+} peak frequency (middle left), duration (middle right) and amplitude (right) as a function of η, in d1s3a107b1 (blue circle), d1s10a24b1 (orange diamond), d2s6a9b1 (green triangle), d9s4a34b1 (red triangle) and d10s1a2b1 (purple hexagon), cocl=1. Data are represented as mean $\pm$ STD, n=20 for each mesh and cluster size tested.

12

Fig 5: Lines are guides for the eyes. Note that no peaks were detected in simulations in d1s8a22b1. (D) Quantification of IP_3R opening frequency (left), Ca^{2+} peak frequency (middle left), duration (middle right) and amplitude (right), in d1s10a24b1, for η=1, 6 and 12 and various levels of neuronal stimulation: IP_3 infused i=50, 100, 150 and 200 (from left to right, light red to dark red), n=20 for each parameter set tested. (E) Scatterplots presenting the variation of IP_3R opening frequency (left), Ca^{2+} peak frequency (middle left), duration (middle right) and amplitude (right) for η=18-24, normalized with Ca^{2+} peak characteristics measured for η=1, as a function of $SVR_{ER/PAP}$. Plots are accompanied by univariate kernel density estimation curves and a linear regression fit. Spearman correlation coefficient, r, and p-value, p, are displayed onto each regression plot.

for i=150, and p=0.026 for i=200) with IP_3R cluster size for i=150 and 200, while cluster size did not affect peak amplitude (ANOVA, p=0.27 for i=50 and p=0.08 for i=100), frequency (ANOVA, p=0.86 for i=50 and p=0.72 for i=100) and duration (p=0.13 for i=50 and p=0.15 for i=100) for i=50 and 100. This effect was mediated by an increased IP_3R opening frequency with cluster size when neuronal stimulation was larger (ANOVA, p= 0.024, $5.23e^{-7}$ and $7.8e^{-5}$, for i=100, 150 and 200, respectively), while clustering had no effect on IP_3R opening frequency for milder neuronal stimulation (ANOVA, p=0.21, i=50). This suggests that IP_3R clustering in PAPs could act as an amplifier of neuronal stimulation.

Unexpectedly, the PAPs in which an IP_3R clustering effect was observed were not the PAPs with the highest ER surface area S_{ER}, i.e with the highest number of IP_3R channels. Indeed, although the normalized IP_3R opening frequency and Ca^{2+} peak frequency at high cluster size were positively correlated with S_{ER}, normalized Ca^{2+} peak amplitude and duration were not correlated with S_{ER} (Supplementary Fig. S3). Rather, normalized IP_3R opening frequency, Ca^{2+} peak amplitude and duration were positively correlated to the ratio between ER surface area and PAP volume $SVR_{ER/PAP}$ (Fig. 5E, p=0.0038, 0.012 and 0.0013, respectively). Ca^{2+} peak frequency however did not vary with $SVR_{ER/PAP}$ (Fig. 5E, p=0.69). This probably results from our peak definition. Indeed, as a peak is considered terminated when the Ca^{2+} trace decreases below peak threshold, a higher frequency of IP_3R opening events can result in successive opening events occurring before peak termination, resulting in a similar peak frequency but larger peak duration.

Overall, our simulation results nuance the effect of the clustering of Ca^{2+} channels on Ca^{2+} signals in small sub-cellular compartments like PAPs. Strikingly, in contrast with reports from models in 2 spatial dimensions [23, 58], Ca^{2+} activity increased with cluster size in only a subset of the realistic 3D PAP meshes tested, highlighting the complex interplay between the ER surface to PAP volume ratio, the intensity of neuronal stimulation and IP_3R clustering on Ca^{2+} microdomain activity. This highlights the importance of cautious interpretation of simulation results on geometrical effects depending on the geometry used.
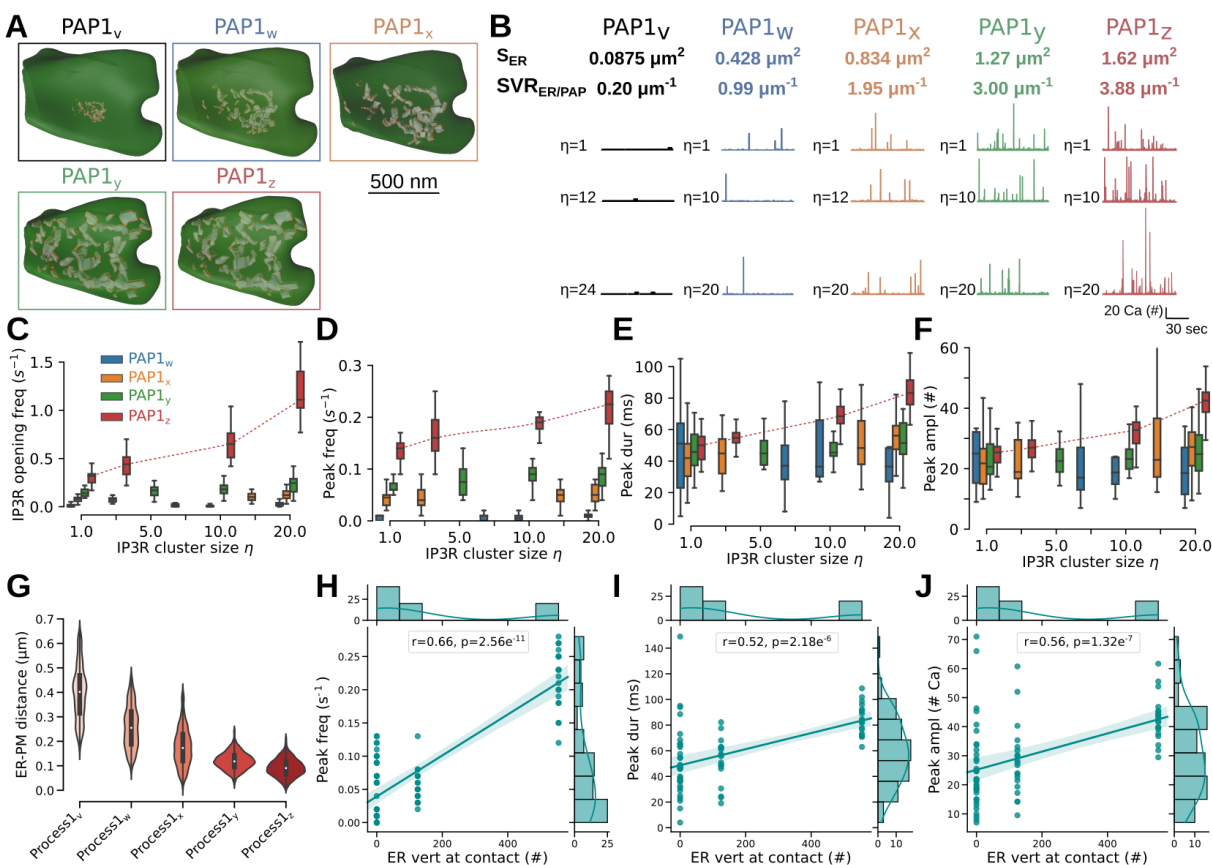
13

The surface-volume ratio of the ER conditions the amplification of Ca^{2+} activity by IP_3R clustering in 3D

Our simulation results revealed that the increase of Ca^{2+} activity resulting from IP_3R clustering increased with the ratio between the ER surface area and the PAP volume ($SVR_{ER/PAP}$, Fig 5E). In the PAP meshes studied in Fig. 5, $SVR_{ER/PAP}$ varied together with PAP shape and ER shape. To discern the effect of ER and PAP shape from $SVR_{ER/PAP}$ on Ca^{2+} activity in PAPs, we created meshes with various ER size and constant ER and PAP shapes. The original mesh was extracted from the 220 μm^3 astrocytic volume, located at the vicinity of the d9s3a51b1 PSD and referred to as PAP1. The location of PAP1 in the 220 μm^3 reconstructed hippocampal astrocytic volume is presented in Supplementary Fig. S4. Meshes with various $SVR_{ER/PAP}$ were created from PAP1 by rescaling the ER using Blender software. Meshes were then created following the mesh pre-processing workflow described in Fig. 4C, resulting in the creation of $PAP1_v$, $PAP1_w$, $PAP1_x$, $PAP1_y$ and $PAP1_z$ meshes (Fig. 6A). The geometrical properties of those meshes are presented in Table 1.

IP_3R opening frequency, Ca^{2+} peak frequency, duration and amplitude increased with $SVR_{ER/PAP}$ (Fig. 6B-F). This is not surprising as ER surface area increases with $SVR_{ER/PAP}$ in those meshes, thus resulting in an increase of the amount of IP_3R channels with $SVR_{ER/PAP}$. The total number of IP_3R channels, N_{IP3R}, thus was 24, 120, 240, 360 and 460, in $PAP1_v$, $PAP1_w$, $PAP1_x$, $PAP1_y$ and $PAP1_z$ meshes, respectively. Importantly, Ca^{2+} peak frequency (Fig. 6D, ANOVA, p=$2.39e^{-8}$), duration (Fig. 6E, ANOVA, p=$7.52e^{-17}$) and amplitude (Fig. 6F, ANOVA, p=$1.29e^{-14}$) increased with IP_3R cluster size in $PAP1_z$ mesh. This resulted from an increase of IP_3R opening frequency with cluster size in $PAP1_z$ (Fig. 6C, ANOVA, p=$5.93e^{-24}$), No clustering effect was observed in $PAP1_{w-y}$ meshes, characterized by a lower $SVR_{ER/PAP}$, confirming the mechanistic link between $SVR_{ER/PAP}$ and the amplification of Ca^{2+} activity mediated by IP_3R clustering suggested in Fig. 5. Note that no Ca^{2+} signals were detected in $PAP1_v$ mesh. Simulations in $PAP1_z$ meshes with constant IP_3R channel number further highlight that this effect results both from the increased number of IP_3R channels in $PAP1_z$ and from ER shape (Supplementary Fig. S5). Supplementary Fig. S6 reveals that IP_3R opening frequency and Ca^{2+} peak frequency increased with $SVR_{ER/PAP}$ even when IP_3R channels were not clustered (η=1).

Increasing ER surface area in PAP1 however also resulted in a decreased distance between the ER and the plasma membrane (PM) in the PAP (Fig. 6G). Importantly, Ca^{2+} peak frequency (Fig. 6H, p=$2.56e^{-11}$), duration (Fig. 6I, p=$2.18e^{-6}$) and amplitude (Fig. 6J, p=$1.32e^{-6}$) increased with the amount of ER vertices at ER-PM contact sites ($\leq$ 20 nm to the closest PM vertex [80, 79]). This suggests that the increased IP_3R clustering effect on Ca^{2+} microdomain activity in $PAP1_z$ could result either from its increased $SVR_{ER/PAP}$ or to the decreased ER-PM distances in this mesh compared to $PAP1_{w-y}$ meshes. Overall, our simulation results suggest that ER shape, notably the ratio between its surface area and PAP volume, shape astrocytic Ca^{2+} microdomain activity at synapses.

14

Fig 6: **The surface-volume ratio of the ER in PAPs conditions the amplification of** Ca^{2+} **activity by** IP_3R **clustering in 3D.** (A) Images of the different PAP meshes created to investigate the effect of the ratio between ER surface area and PAP volume, $SVR_{ER/PAP}$, on Ca^{2+} microdomain activity: $PAP1_{v-z}$. Meshes were obtained by rescaling the ER object in PAP1, located at the vicinity of the d9s3a51b1 PSD (Supplementary Fig. S4). Geometrical features of the meshes are presented in Table 1. (B) Representative free Ca^{2+} traces measured in $PAP1_v$ (black), $PAP1_w$ (blue), $PAP1_x$ (orange), $PAP1_y$ (green) and $PAP1_z$ (red), for IP_3R cluster size $\eta=1$ (top), $\eta=12$ (middle) and $\eta=24$ (bottom). (C-F) Quantification of IP_3R opening frequency (C), Ca^{2+} peak frequency (D), duration (E) and amplitude (F), in $PAP1_w$ (blue), $PAP1_x$ (orange), $PAP1_y$ (green) and $PAP1_z$ (red), for $\eta=1-23$. Note that η varies depending on the mesh (see Methods). Lines were added to visualize the effect of η on Ca^{2+} peak characteristics in $PAP1_z$ mesh. (G) Quantification of the variation of the distance between each ER vertex and the closest plasma membrane (PM) vertex in $PAP1_{v-z}$ meshes. (H-J) Scatterplots presenting Ca^{2+} peak frequency (H), duration (I) and amplitude (J) in $PAP1_{v-z}$ meshes for $\eta=20$, as a function of the number of ER vertices ≤ 20 nm to the closest PM vertex.

15

Fig 6: Plots are presented with univariate kernel density estimation curves and a linear regression fit. Spearman correlation coefficient, r, and p-value, p, are displayed onto each regression plot.

Quantification of ER-PM distance distribution within PAPs

As simulation results suggested that Ca^{2+} activity in $PAP1_{v-z}$ meshes varies depending on the distribution of the ER within the PAP, we next aimed at quantifying ER distribution in the twenty ER-containing PAP meshes reconstructed from EM and presented in Fig. 3. To do so, we measured the distance between each vertex on the plasma membrane (PM) and the closest vertex on the ER. We found that ER-PM distance is highly variable in PAPs from a single cell, with an average ER-PM distance within a single PAP from around 200 nm to 1200 nm (Fig. 7B-C). Not surprisingly, mean ER-PM distance decreases as ER (Fig. 7D, p=$5.01e^{-10}$) and PAP (Fig. 7E, p=0.055) surface area increase. Interestingly, ER-PM distance was lower in PAPs contacting boutons with higher surface area (Fig. 7F, p=0.022). Note that there was no correlation between ER-PM distance and spine surface area (Fig. 7G, p=0.73). Importantly, we found that PAPs closer to the synapse are characterized by lower mean ER-PM distance (Fig. 7H, p=$2.2e^{-5}$), which, according to simulation results presented in Fig. 6, could result in enhanced Ca^{2+} activity in those PAPs.

Effect of ER-PM distance in PAPs on Ca^{2+} microdomain activity

To discern the effect of $SVR_{ER/PAP}$ from the effect of ER-PM distance on Ca^{2+} microdomain activity in PAPs reported in Fig. 6, we implemented an algorithm that creates realistic tetrahedral 3D meshes of PAPs characterized by various distributions of the ER within the same PAP. The workflow is presented in Fig. 8. Briefly, the ER is split into small portions of similar size, then resized to match the total ER surface area of the original mesh. Simulations in meshes with the original ER and with split ER confirmed that this ER splitting algorithm does not alter Ca^{2+} activity in the PAP (Supplementary Fig. S7). A simulation of n frames is then generated in Blender, which alters the location of the ER objects within the PAP. Each frame is thus characterized by a unique distribution of the ER objects within the PAP, while ER and PAP shape, surface area, volume and SVR are constant across frames (Supplementary movie 3). The mesh processing workflow presented in Fig. 4C is then automatically applied to each frame of interest. This workflow allows the creation of numerous realistic 3D PAP meshes, that can be used for reaction-diffusion simulations in 3D. Fig. 7B-D displays the quantification of ER distribution in the PAP meshes created with this workflow on PAP d1s15a32b1. The workflow successfully produced realistic tetrahedral PAP meshes characterized by various ER-PM distances (Fig. 7B). Note that the distribution of ER-PM distance at ER-PM contact sites (ER-PM distance $\leq$ 20 nm) did not vary, while the number of ER vertices belonging to contact sites, and thus the size of the contact sites, increased with frame number (Fig. 7C).

16
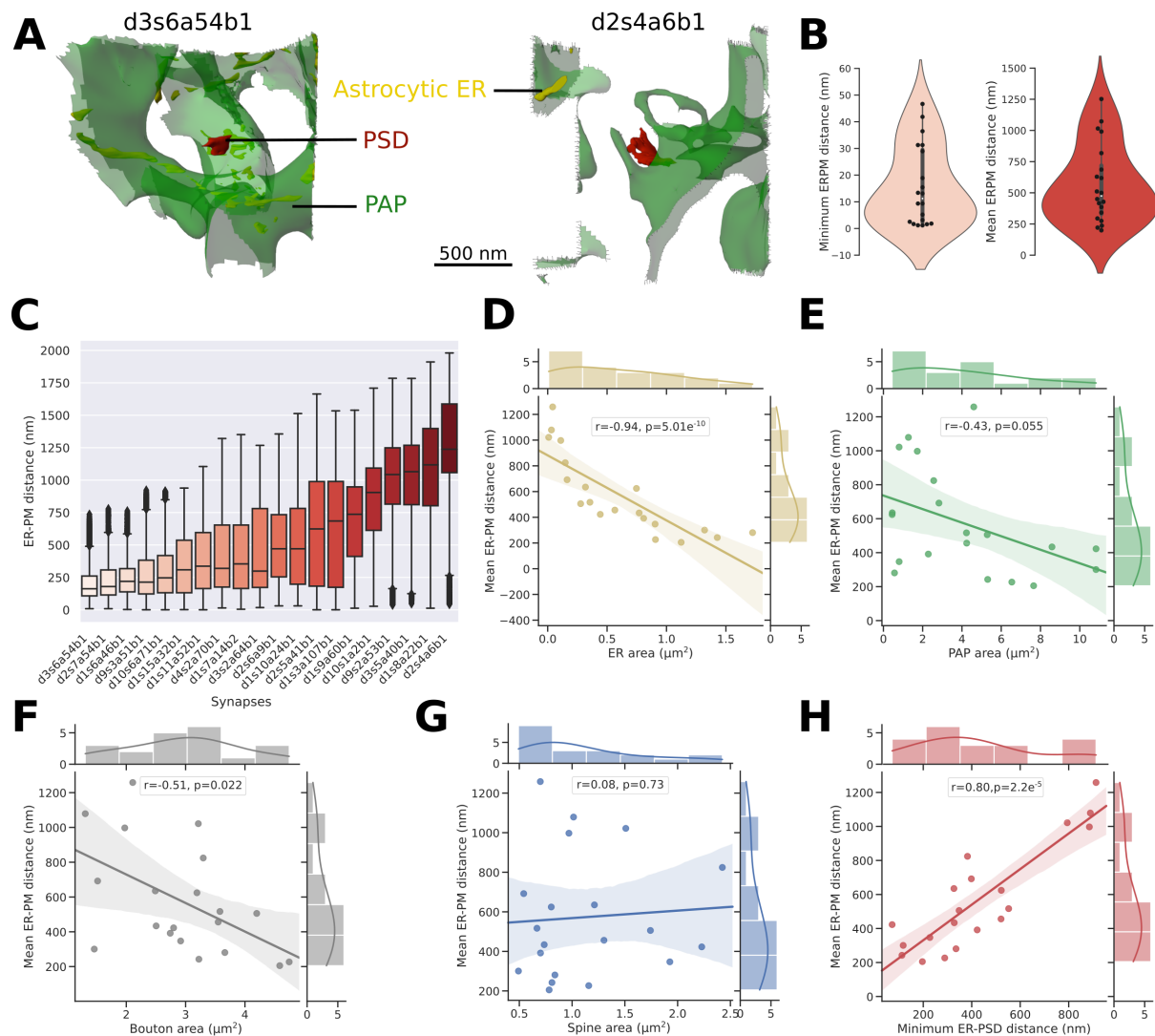
Fig 7: **ER-PM distance in PAPs is highly variable and is decreased in PAPs close to the synapse.** (A) Images of 2 PAP meshes (green), d3s6a54b1 (left) and d2s4a6b1 (right) with the neighboring PSD (red), displaying the diverse shapes and distributions of the ER (yellow) in PAPs from the same cell. (B) Distribution of the minimum (left) and mean (right) distance between each vertex on the plasma membrane (PM) and the closest ER vertex, measured in PAP meshes reconstructed from EM, n=20 (Fig. 3). (C) Quantification of the distance between each PM vertex and the closest ER vertex in each PAP mesh. (D-F) Scatterplots presenting the variation of the mean distance between each PM vertex and the closest ER vertex as a function of the surface area of the ER (D), PAP (E), bouton (F), and spine (G), and as a function of the minimum ER-PSD distance (H), n=20. Plots are presented with univariate kernel density estimation curves and a linear regression fit. Spearman correlation coefficient, r, and p-value, p, are displayed onto each regression plot.

17

To test the effect of ER distribution in PAPs, simulations were performed in meshes from frames 0, 21, 64 and 250 of PAP d1s15a32b1 (Fig. 9A) with different IP_3R cluster sizes, η. Free Ca^{2+} signals did not vary depending on ER distribution within the PAP (Fig. 9C). Interestingly, ER distribution did not affect the amplification of IP_3R opening frequency (ANOVA, p=0.059), Ca^{2+} peak duration (ANOVA, p=0.55) and amplitude (ANOVA, p=0.15) with IP_3R cluster size when IP_3R clusters were randomly distributed on the membrane of the ER (Fig. 9D). However, the increase of peak frequency with cluster size was larger in meshes in which the ER was closer to the plasma membrane (Fig 9D, ANOVA, p=0.0048). This suggests that a distribution of the ER closer to the plasma membrane might allow increased Ca^{2+} peak frequency with IP_3R cluster size.

As IP_3R clusters are believed to be preferentially located at ER-PM contact sites [72], we performed simulations in the same meshes while positioning IP_3R clusters at ER-PM contact sites. Screenshots of simulations with different locations of IP_3R clusters are presented in Fig. 9B. Interestingly, locating IP_3R clusters at ER-PM contact sites resulted in larger increases of IP_3R opening frequency (ANOVA, p=0.0019) and Ca^{2+} peak frequency (ANOVA, p=0.0043) with cluster size in meshes in which the ER was closer to the PM (Fig. 9D). However, the location of the ER did not impact the effect of IP_3R cluster size on Ca^{2+} peak duration (ANOVA, p=0.45) and amplitude (ANOVA, p=0.069). Together, those results suggest that a distribution of the ER closer to the plasma membrane, coupled with a location of IP_3R clusters at ER-PM contact sites, favors an increase of Ca^{2+} peak frequency with cluster size. ER-PM contact sites could act as diffusional barriers. Locating IP_3R channels at ER-PM contact sites would thus increase the residency time of Ca^{2+} ions and IP_3 molecules at the vicinity of the channels, thus increasing the probability of Ca^{2+} and IP_3 binding to IP_3Rs and resulting in an increased IP_3R opening frequency in meshes with larger ER-PM contact sites. To further test the interplay between ER distribution, IP_3R clustering and local diffusional properties, Ca^{2+} buffers, here Ca^{2+} indicators GCaMP6s, were added to the model. Strikingly, ER distribution had a greater effect on buffered Ca^{2+} signals compared to free Ca^{2+} signals (Fig. 9E). More precisely, the increase of IP_3R opening frequency (ANOVA, p=$2.37e^{-7}$), Ca-GCaMP peak frequency (ANOVA, p=$1.14e^{-4}$), duration (ANOVA, p=$7.78e^{-3}$) and amplitude (ANOVA, p=0.023) with IP_3R cluster size was significantly larger in meshes in which the ER was located closer to the plasma membrane. Those results highlight that the effect of ER distribution within the PAP on Ca^{2+} microdomain activity is conditioned by the location of IP_3R channels at ER-PM contact sites and by local Ca^{2+} buffering.

Discussion

Here, we extracted 3D meshes of tripartite synapses from a 220 μm^3 hippocampal astrocytic volume from the CA1 stratum radiatum region, reconstructed from EM [17]. Quantification
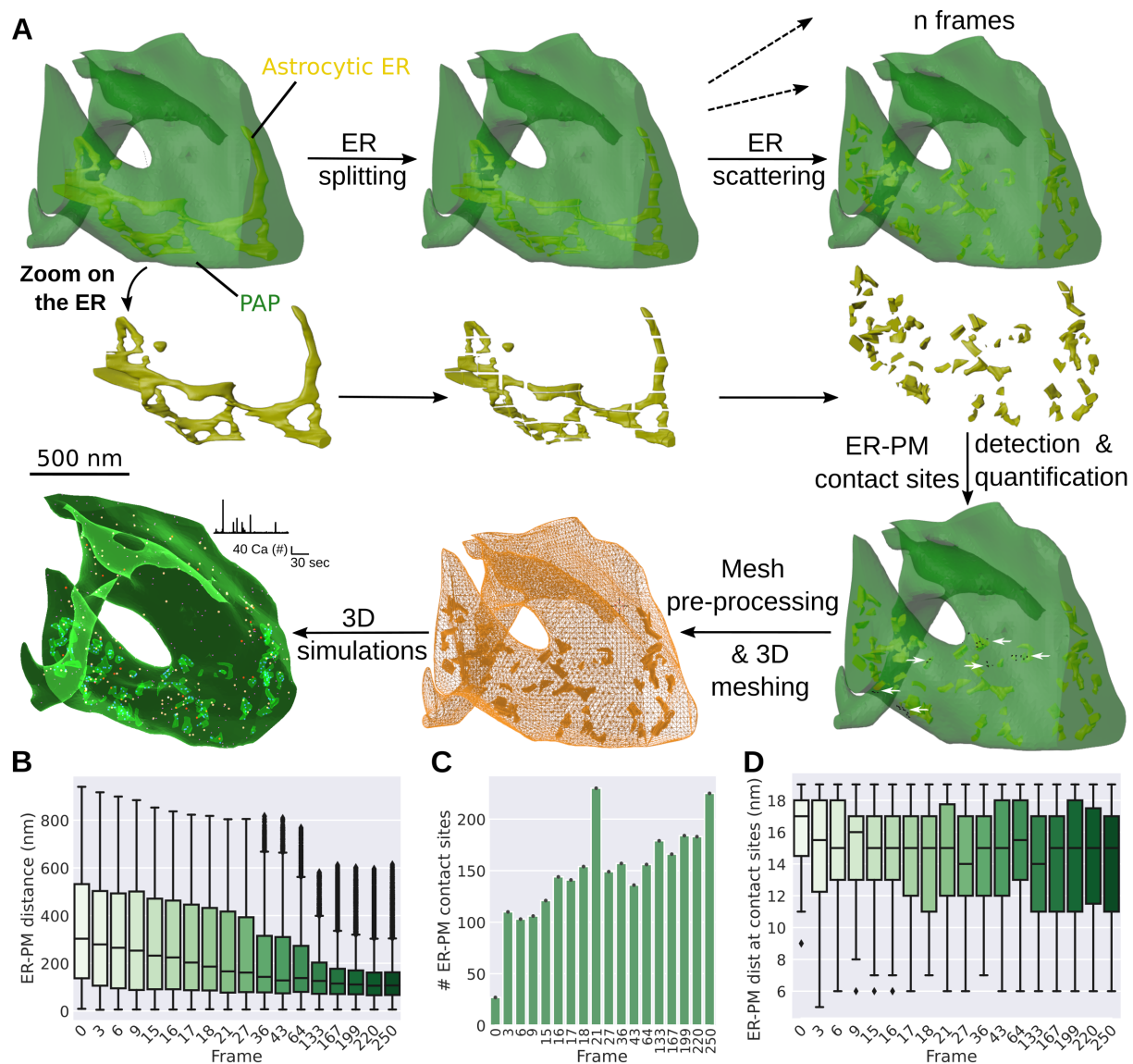
Fig 8: **Automated realistic 3D PAP mesh generation with diverse ER distributions.** (A) Schematic representing the workflow developed in this study to create realistic PAP meshes in 3 spatial dimensions with various ER distributions and constant shape, volume and surface area of PAP and ER, used on the PAP mesh d1s15a32b1. The ER is split and a simulation with n frames is generated in Blender, in which ER objects are subject to physical forces that alter their spatial distribution. The n frames are thus characterized by different locations of the ER elements within the PAP, with constant ER and PAP shapes. The pipeline detects, quantifies and exports in a text file the distance between each vertex at the plasma membrane (PM) and the closest vertex at the membrane of the ER. A point cloud can be created to visualize the ER vertices at ER-PM contact sites (ER-PM distance ≤ 20 nm, white arrows). The mesh pre-processing workflow presented in Fig. 4C is then applied to the mesh of each desired frame. The resulting 3D tetrahedral meshes can then be used for 3D reaction-diffusion simulations.

19

Fig 8: (B) Quantification of the distance between each PM vertex and the closest ER vertex in the meshes generated by the workflow presented in panel A, applied to the d1s15a32b1 PAP mesh. (C) Quantification of the number of ER vertices located at ER-PM contact sites, i.e $\leq$ 20 nm to the closest PM vertex, in each frame from mesh d1s15a32b1. (D) Quantification of the distance between each PM vertex and the closest ER vertex at ER-PM contact sites, in each frame from mesh d1s15a32b1.

of the geometrical features of those meshes highlighted the diverse geometrical properties of PAPs from a single astrocyte and revealed, contrary to a widespread belief that PAPs are devoid of ER [55, 59], that 75 % of PAPs contained some ER. Interestingly, we found that PAPs are the closest to the synapse when bouton surface area is low, which could result from the spatial constraints imposed by larger boutons, preventing the PAP from getting in close contact to the PSD. Reaction-diffusion simulations in the realistic PAP 3D meshes reconstructed in this study provided key insights into the effect of the diverse shapes and distributions of the ER in PAPs on microdomain Ca^{2+} activity. As reactive astrocytes, hallmark of brain diseases [26], are characterized by a remodelling of ER volume and shape [39], our results suggest that such geometrical alterations of the ER could be one of the factors responsible for the altered astrocytic Ca^{2+} activity reported in pathological conditions [65].

Fine-tuning the spatial distribution of Ca^{2+} channels, monitoring channel opening events at each channel, while independently manipulating ER shape and distribution, such as performed in this study, is not feasible experimentally. It is yet essential to understand the mechanistic link between the spatial features of the astrocyte and its Ca^{2+} microdomain activity. Combining our detailed biophysical model of Ca^{2+} signals in PAPs, the PAP meshes that we extracted from EM and the realistic PAP meshes with various ER distributions generated by our automated mesh generator allowed us to provide key insights into Ca^{2+} signaling in PAPs. Notably, we predict how the complex interplay between the clustering of Ca^{2+} channels, the ratio between ER surface surface area and PAP volume, Ca^{2+} buffering and the size and location of ER-PM contact sites shapes Ca^{2+} microdomain signals at tripartite synapses. This study is the first to our knowledge to model Ca^{2+} activity in astrocytes with realistic shapes in 3D at the nanoscale that accounts for the complex and diverse spatial characteristics of Ca^{2+} stores in PAPs. Furthermore, our results highlight the impact of the modeling choices on simulation results, notably when investigating spatial effects. Importantly, our results nuance the effect of the clustering of Ca^{2+} channels, which is stronger in 2D or simple 3D shapes than in more realistic 3D meshes. This is crucial as, until now, modeling studies on PAPs were conducted in 1D, 2D or in simple 3D shapes, notably cylinders [47, 24, 13, 20, 22, 32]. The 3D meshes provided by this study, together with our realistic 3D PAP mesh generator, pave the way for future modeling studies in realistic 3D meshes to investigate the mechanisms governing neuron-astrocyte communication at tripartite synapses.

20
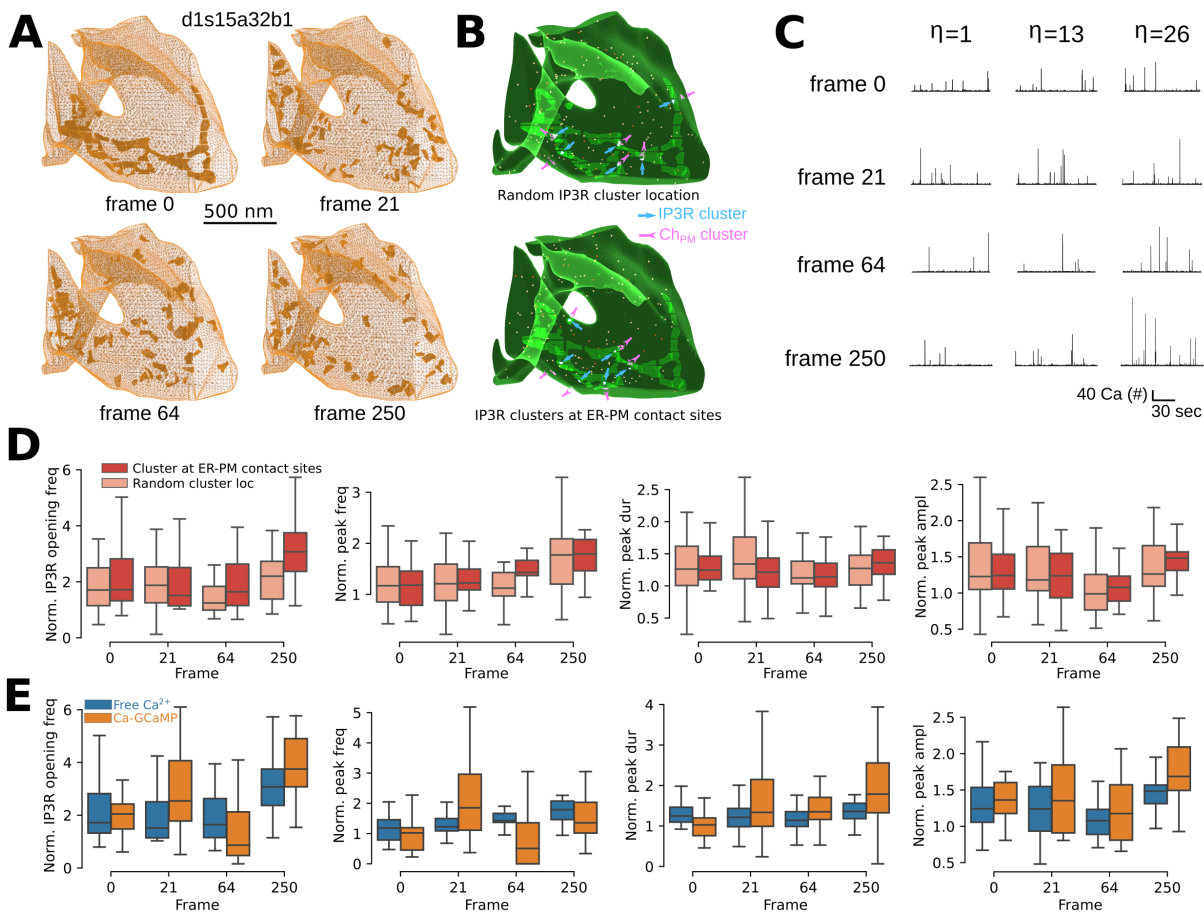
Fig 9: Ca^{2+} **buffering and** IP_3R **channel location mediate the effect of ER-PM distance on** Ca^{2+} **microdomain activity in PAPs.** (A) Images presenting different meshes created from PAP d1s15a32b1 using the automated workflow presented in Fig. 8: frames 0, 21, 64 and 250, characterized by diverse ER distributions within the PAP with constant PAP and ER shape, volume and surface area. Characteristics of ER-PM distance in those meshes are displayed in Fig. 8B-D. (B) Screenshots of simulations performed in $d1s15a32b1_{f0}$ mesh (frame 0), with IP_3R clusters (blue, arrows) distributed randomly on the ER membrane (top) or at ER-PM contact sites (bottom). IP_3R clusters were co-localized with Ch_{PM} clusters at the plasma membrane (purple, inverse arrows): cocl=1. (C) Representative free Ca^{2+} traces in frames 0, 21, 64 and 250, with IP_3R cluster size η=1, 13 and 26 and random distribution of IP_3R clusters on the ER. (D) Quantification of IP_3R opening frequency (left), Ca^{2+} peak frequency (middle left), duration (middle right) and amplitude (right), in frames 0, 21, 64 and 250, for η=26, normalized by Ca^{2+} peak characteristics for η=1 in each mesh, with IP_3R clusters at random locations on the ER (left, light red) or at ER-PM contact sites (right, dark red).

21

Fig 9: (E) Quantification of IP$_3$R opening frequency (left), peak frequency (middle left), duration (middle right) and amplitude (right) of free Ca^{2+} signals (blue) and Ca-GCaMP signals (orange), in frames 0, 21, 64 and 250, for η=26, normalized by Ca^{2+} peak characteristics for η=1. IP$_3$R clusters were located at ER-PM contact sites. n=20 for each parameter set tested.

The geometrical data used here were extracted from electron microscopy, which is the only tool that can resolve PAP and ER shape at a high spatial resolution (6 nm here), yet results in potential alterations of the ultrastructure of the extracellular space [42] and cannot be used to study live cells. Furthermore, the model used in this study, focusing on the effect of the ER shape and distribution on Ca^{2+} activity, describes with great details the kinetics of ER-mediated Ca^{2+} signals while simplifying other Ca^{2+} sources. Other Ca^{2+} sources and channels however contribute to Ca^{2+} microdomain activity in PAPs, including mitochondria, the Na^+/Ca^{2+} exchanger, transient receptor potential ankyrin 1 channels, L-type voltage gated channels and other pathways [64, 62]. According to our model's predictions, the spatial distribution of Ca^{2+} channels can alter the spatio-temporal properties of Ca^{2+} microdomain signals in PAPs as well as their amplification upon neuronal stimulation. Further quantification of the Ca^{2+} channels expressed in PAPs, their density, location and remodeling in live tissue under (patho-)physiological conditions is thus essential to better understand astrocyte activity at synapses. The recent advances in super-resolution techniques, notably single particle tracking methods, provide a promising avenue to overcome current limitations in obtaining such data [33, 6].

Recent super-resolution studies in live neurons revealed dynamical remodeling of ER-PM contact sites [27] and diffusional trapping of molecules resulting from the ER remodeling [18] in neurons. Those observations, together with our model predictions, highlight the need for further quantification of the dynamical shape and distribution of the ER in astrocytes in live tissue to fully grasp its influence on Ca^{2+} microdomain activity in astroytes. According to our model predictions, preferential location of IP$_3$Rs at ER-PM contact sites might be essential to allow signal amplification with IP$_3$R cluster size and could thus strongly alter the spatio-temporal properties of astrocytic Ca^{2+} signals evoked by neurotransmitters, potentially affecting the subsequent modulation of neuronal activity by astrocytes. Our results, in accordance with previous computational studies in other cell types [81], highlight that Ca^{2+} buffering plays a crucial role in shaping Ca^{2+} activity at ER-PM contact sites. The Ca^{2+} buffering effect described here was mediated by Ca^{2+} indicators. Future experimental and computational studies will be essential to assess Ca^{2+} buffering mechanisms in astrocytes and PAPs, which are still poorly understood, yet, according to our simulation results, play crucial roles in shaping Ca^{2+} microdomain activity in astrocytes.

Overall, this study provides new insights into astrocytic activity at tripartite synapses by characterizing the presence, shape and distribution of the ER in PAPs and by shedding light to the mechanistic link between those features and microdomain Ca^{2+} activity at tripartite

22

synapses. The realistic 3D meshes of tripartite synapses created in this study pave the way for new modeling studies of neuron-astrocyte communication in the synaptic micro-environment, allowing the study of various processes, such as glutamate spillover or gliotransmission. Such studies will be crucial to decipher whether the various nano-architectures displayed by tripartite synapses reflect distinct functional identities.

Methods

3D reconstruction from electron microscopy

Sample preparation and imaging

The original dataset used in this work (EM stack and 3D reconstructions) was previously published in [17]. The block was a gift from Graham Knott (BioEM imaging facility at EPFL, Lausanne, Switzerland). All procedures were performed according to the Swiss Federal Laws. One P90 Sprague-Dawley rat was deeply anesthetized with isoflurane and transcardially perfused using 2% paraformaldehyde and 2.5% glutaraldehyde in PBS 0.1M. Coronal sections (100 μm) were obtained and washed in cacodylate buffer, followed by a post-fixation using osmium tetroxide and uranyl acetate. Finally, the sections were embedded in Durcupan. Regions of the hippocampus were dissected under a stereoscopic microscope, mounted onto a blank resin slab, and trimmed using an ultramicrotome (Laica Ultracut UC-7). Imaging was performed using an NVision 40 FIB-SEM (Carl Zeiss) with an acceleration voltage of 1.5 kV, a current of 350 pA, and a dwell time of 10 μs/pixel. Serial images were obtained using backscattered electrons and collected at a 6 nm/pixel magnification and 5 nm of milling depth between images.

3D reconstruction and rendering

The serial micrographs were first registered using Multistackreg, a freely available plug-in for Fiji [17]. Then, using those micrographs, we proceeded to the image segmentation and 3D model reconstructions by using TrackEM2 (a plug-in for Fiji) for manual segmentation, and iLastik, for a semi-automated segmentation. The extracted models were then imported to Blender software for visualization and rendering purposes [16].

Extraction of tripartite synapse meshes

For each synapse in contact with the 220 μm^3 astrocytic volume, a cube of edge length $1.5\mu m$ (3.375 μm^3) was created and centered at the center of mass of the PSD. All the elements of the mesh (astrocyte, astrocytic ER, spine and bouton) that were within the cubic volume were isolated using a boolean intersection operator available in Blender, forming what we refer to as a tripartite synapse mesh. The size of the cube was chosen to be large enough to contain the

23

whole spine and bouton elements while containing a single synapse, taking into consideration that the neuropil is believed to contain around one synapse per micrometer cube. This workflow resulted in the creation of 44 excitatory and 2 inhibitory synapse meshes.

3D mesh manipulation

All 3D mesh manipulations were performed with open-access, open-source software. All 3D PAP meshes used in this study will be available online upon paper acceptance.

3D PAP mesh processing for reaction-diffusion simulations

PAP meshes from tripartite synapse meshes were pre-processed using Blender software so that they could be used for reaction-diffusion simulations. The workflow is illustrated in Fig. 4C. Intersection between ER and PAP membranes was prevented by using a boolean intersection operator. ER was relocated a few nanometers away from the plasma membrane. PAP compartments that did not belong to the main PAP volume were deleted. Boolean difference operation between PAP and ER elements was performed. Non-manifold vertices were repaired. The resulting PAP mesh was exported in .stl format, which was then converted into a .msh 3D tetrahedral mesh using TetWild software [38]. Lastly, the mesh was imported into Gmsh software to be converted into 2.2 ASCII format, format supported by the STEPS mesh importer.

Automated 3D PAP mesh generation

We have implemented a workflow to generate realistic 3D tetrahedral PAP meshes characterized by various ER locations and constant ER shape. The algorithm is written in python, can be imported in Blender and is available at https://bit.ly/3Nc2Qin. The workflow is presented in Fig. 8. First, all elements of the mesh, i.e the PAP and the ER, are relocated so that their center of mass is centered at the origin. Then, the ER is split into smaller ER objects using a custom-made function. Briefly, n cubes of a given size are placed along the ER object. Intersection boolean operation is then performed between the ER and each cube, resulting in the creation of n ER objects. ER objects smaller than 30 nm^3 are deleted. The remaining ER objects are rescaled so that the sum of their surface areas matches the area of the original ER element, measured with the Blender 3D Print add-on. The number and size of cubes can be altered depending on the size of the original ER and on the mesh characteristics desired. Using Blender's physics engine, a simulation with n frames is generated, in which ER objects are subject to physical forces that alter their location between each frame. Inputs of the 'RunPhysics' function include parameters that affect how close objects can get, which can be altered to prevent membrane intersection. Note that successful scattering of the ER depends on the geometrical properties of each mesh so that adjusting the parameters of physics simulation might be necessary depending on the mesh used. Details are provided in comments of the code to allow the user to adjust the code to the mesh under study. Examples of frames generated by this workflow applied to

24

480   d1s15a32b1 PAP mesh are presented in Supplementary movie 3. For each selected frame, the
481   mesh pre-processing steps presented in Fig. 4C are performed automatically, resulting in the
482   export of a .stl triangular mesh. 3D meshing and format conversion can then be performed using
483   TetWild and Gmsh software, as described above. The resulting meshes can be used to perform
484   reaction-diffusion simulations.

Analysis of the geometrical properties of 3D meshes

486   The volume and surface area of each synaptic element, i.e the PAP, astrocytic ER, spine and
487   bouton, were measured using the Blender add-on Neuromorph [40]. We implemented a python
488   script that can be imported in Blender software that measures distances between mesh elements
489   of interest. The distance between each vertex of the plasma membrane of the PAP and the
490   center of mass of the neighboring PSD was computed in Blender and stored in a list. Similarly,
491   ER-PSD distance was quantified by measuring the distance between each vertex of the ER
492   membrane and the center of mass of the PSD. To characterize ER-PM distance, for each vertex
493   on the PM, the closest ER vertex was detected and its distance to the PM vertex was stored in
494   a list. PM-PSD, ER-PSD and ER-PM distance lists were exported to a text file for analysis and
495   visualisation. The analysis code, implemented in python and imported in Blender, is available
496   at https://bit.ly/3Nc2Qin.

Computational modeling

Modeled reactions and computational approach

499   Astrocytic Ca^{2+} signals in PAPs were simulated using the reaction-diffusion voxel-based model
500   of ER-dependent Ca^{2+} signaling from Denizot and colleagues ([20] Table 2, Fig. 6-7). Briefly,
501   the model describes Ca^{2+} fluxes in and out of the astrocytic cytosol. The opening of IP_3R
502   channels on the ER membrane triggers Ca^{2+} influx in the cytosol. IP_3 can be synthesized
503   by the Ca^{2+}-dependent activity of Phospholipase C (PLC) δ. IP_3 removal from the cytosol is
504   described by a decay rate. IP_3R dynamics is derived from the De Young & Keizer's model
505   [19]. Each IP_3R has 3 binding sites: one to IP_3 and two to Ca^{2+} (activating and inhibiting).
506   The channel can thus be in 8 different states. The open state is {110}: IP_3 and Ca^{2+} bound
507   to the activating sites and the Ca^{2+} inactivating site is unbound. In a subset of simulations,
508   GCaMPs6s, genetically-encoded Ca^{2+} indicators [64], were added to the cytosol and variations
509   of [Ca-GCaMP] concentration, mimicking experimental Ca^{2+} imaging, were measured. For
510   further details on the kinetic scheme, parameter values and model assumptions, please refer to
511   the original paper presenting the model [20]. We slightly altered this model to better describe
512   and control IP_3R-independent Ca^{2+} fluxes. To do so, IP_3R-independent Ca^{2+} influx was mod-
513   eled as an influx through Ca^{2+} channels at the plasma membrane, Ch_{PM}. For simplicity, the
514   amount of Ch_{PM} channels equals the total number of IP_3R channels, N_{IP3R}. Ca^{2+} influx rate
515   at Ch_{PM} channels, $\gamma_{ch_{PM}}$, is $15 \times 10^{-8} s^{-1}$. The reactions modeled here are illustrated in Fig. 4A.
516

The model was implemented using the STochastic Engine for Pathway Simulation (STEPS) python package (http://steps.sourceforge.net/) [36]. This software uses a spatialized version of Gillespie's SSA algorithm [31] to perform exact stochastic simulations of reaction-diffusion systems. Simulations in STEPS allow the diffusion of molecules in 3D tetrahedral meshes and onto the surfaces of the mesh, such as the ER and plasma membrane. STEPS allows volume and surface reactions. Reactions can only occur between molecules within the same tetrahedron (volume reactions) or in adjacent triangle and tetrahedron (surface reactions). Boundary conditions were reflective. Simulation time was 100s. The states and amounts of all molecular species were measured at each time step (1 ms).

Neuronal stimulation simulation

Unless specified otherwise, glutamatergic transmission at the synapse was modeled and occurred at simulation time t=1s. To do so, IP_3 molecules were injected in tetrahedra below the plasma membrane of the PAP, emulating IP_3 synthesis resulting from the activation of metabotropic glutamatergic receptors at the membrane of the PAP. Supplementary movie 4 presents a visualization of a simulation at neuronal stimulation time, in the d2s6a9b1 PAP mesh.

Ca^{2+} channel clustering algorithm

Surfaces correspond to triangular meshes. To simulate IP_3R clustering, N_{IP3R}/η IP_3R clusters were randomly positioned onto the membrane of the ER, where N_{IP3R} is the total number of IP_3Rs and η is the number of channels per cluster. As η is an integer, it must be a divider of N_{IP3R}. As IP_3R density was kept constant across simulations, $3.5e^{-3}/\mu m^2$ [20], the total number of IP_3Rs, N_{IP3R}, and IP_3R cluster size η varied depending on the mesh. Each IP_3R cluster was located within a region of interest, as defined in STEPS, consisting in 4 triangles. Clusters could not overlap. In a subset of simulations, IP_3R clusters were located at ER-PM contact sites. To do so, ER triangles were sorted depending on the distance between their center of mass and the closest PM triangle. Cluster center was then located at the ER triangle in which no cluster was already located characterized by the lowest ER-PM distance in the mesh. The cluster ROI consisted in this cluster center triangle and the neighboring triangles. Similarly, clusters could not overlap. The number of IP_3R opening events at each cluster ROI was measured at each time step.

IP$_3$R channels were co-clustered with Ch_{PM} Ca^{2+} channels at the plasma membrane (cocl=1), unless specified otherwise. If cocl=0, Ch_{PM} channels were randomly distributed onto the plasma membrane. If cocl=1, Ch_{PM} channels were co-clustered with IP_3Rs. To do so, Ch_{PM} cluster center was defined as the triangle on the plasma membrane that was the closest to the IP_3R cluster center triangle on the ER. The cluster ROI then consisted in this Ch_{PM} cluster center and the neighboring triangles. Similarly to IP_3R cluster ROIs, Ch_{PM} clusters could not overlap. For simplicity, Ch_{PM} cluster size was identical to IP_3R cluster size: η.

26

Simulation code

Simulations were performed using the model of Ca^{2+} signals in fine processes from Denizot and collaborators [20], available at http://modeldb.yale.edu/247694. The simulation code used in this study is available at https://bit.ly/3Nc2Qin.

Ca^{2+} peak detection and characterization

Ca^{2+} peaks were considered initiated and terminated when Ca^{2+} concentration increased above and decreased below peak threshold, respectively. Peak threshold was $[Ca]_b + n\sigma_{Ca}$, where $[Ca]_b$ is the basal Ca^{2+} concentration and σ_{Ca} is the standard deviation of the $[Ca^{2+}]$ histogram in the absence of neuronal stimulation. n varied depending on signal/noise ratio of the simulation of interest, notably when measuring Ca-GCaMP signals, noisier than free Ca^{2+} signals (see (e.g.) Fig 4E). Ca^{2+} peak frequency, duration and amplitude were measured in each simulation. Ca^{2+} peak duration corresponds to the time between peak initiation and termination, Ca^{2+} peak amplitude corresponds to the maximum number of Ca^{2+} ions in the cytosol measured within peak duration time and Ca^{2+} peak frequency corresponds to the amount of peaks detected during simulation time. The number of IP_3R peak opening events was recorded at each time step, in the whole cell as well as at each IP_3R cluster ROI.

Statistical analysis

Data analysis and statistics were performed using open-access and open-source software: the SciPy and pandas python libraries. Data visualization was performed using Seaborn and Matplotlib python libraries. Sample size for each analysis, n, is described in the figure legend. Prior to statistical analysis, normality of data distribution was inferred using the Shapiro-Wilk test. Relationship between Ca^{2+} peak characteristics and parameter values was inferred using one-way ANOVA if values followed a Gaussian distribution, Kruskal-Wallis one-way ANOVA otherwise. Note that the effect of IP_3R clustering was quantified by measuring the ratio between the Ca^{2+} peak characteristic of interest measured at a given IP_3R cluster size, $\eta > 1$ and its mean value for $\eta=1$. The linear relationship between two datasets was evaluated using Spearman's correlation coefficient. The test and p-value, p, associated with each analysis is described in the figure legend or in the main text.

References

[1] Amina Aboufares El Alaoui, Molly Jackson, Mara Fabri, Luisa de Vivo, and Michele Bellesi. "Characterization of Subcellular Organelles in Cortical Perisynaptic Astrocytes". English. In: *Frontiers in Cellular Neuroscience* 14 (2021). Publisher: Frontiers.

27

[2]   Amit Agarwal et al. "Transient Opening of the Mitochondrial Permeability Transition Pore Induces Microdomain Calcium Transients in Astrocyte Processes". English. In: *Neuron* 93.3 (Feb. 2017), 587–605.e7.

[3]   Alfonso Araque, Giorgio Carmignoto, Philip G. Haydon, Stéphane H. R. Oliet, Richard Robitaille, and Andrea Volterra. "Gliotransmitters travel in time and space". eng. In: *Neuron* 81.4 (Feb. 2014), pp. 728–739.

[4]   Alfonso Araque, Vladimir Parpura, Rita P. Sanzgiri, and Philip G. Haydon. "Tripartite synapses: glia, the unacknowledged partner". In: *Trends in Neurosciences* 22.5 (May 1999), pp. 208–215.

[5]   Misa Arizono, V. V. G. Krishna Inavalli, Stéphane Bancelin, Mónica Fernández-Monreal, and U. Valentin Nägerl. "Super-resolution shadow imaging reveals local remodeling of astrocytic microstructures and brain extracellular space after osmotic challenge". en. In: *Glia* 69.6 (2021). _eprint: https://onlinelibrary.wiley.com/doi/pdf/10.1002/glia.23995, pp. 1605–1613.

[6]   Misa Arizono et al. "Nanoscale imaging of the functional anatomy of the brain". en. In: *Neuroforum* (Mar. 2021). Publisher: De Gruyter Section: Neuroforum.

[7]   Misa Arizono et al. "Structural basis of astrocytic Ca 2+ signals at tripartite synapses". en. In: *Nature Communications* 11.1 (Apr. 2020). Number: 1 Publisher: Nature Publishing Group, pp. 1–15.

[8]   Akiko Asada et al. "Subtle modulation of ongoing calcium dynamics in astrocytic microdomains by sensory inputs". eng. In: *Physiological Reports* 3.10 (Oct. 2015).

[9]   Aina Badia-Soteras et al. *Proximity of astrocyte leaflets to the synapse determines memory strength*. en. Tech. rep. Section: New Results Type: article. bioRxiv, Jan. 2022, p. 2022.01.30.478393.

[10]   L. H. Bergersen et al. "Immunogold Detection of L-glutamate and D-serine in Small Synaptic-Like Microvesicles in Adult Hippocampal Astrocytes". en. In: *Cerebral Cortex* 22.7 (July 2012), pp. 1690–1697.

[11]   Yann Bernardinelli et al. "Activity-dependent structural plasticity of perisynaptic astrocytic domains promotes excitatory synapse stability". eng. In: *Current biology: CB* 24.15 (Aug. 2014), pp. 1679–1688.

[12]   Erika Bindocci, Iaroslav Savtchouk, Nicolas Liaudet, Denise Becker, Giovanni Carriero, and Andrea Volterra. "Three-dimensional Ca^{2+} imaging advances understanding of astrocyte biology". en. In: *Science* 356.6339 (May 2017), eaai8185.

[13]   Kevin Breslin et al. "Potassium and sodium microdomains in thin astroglial processes: A computational model study". en. In: *PLOS Computational Biology* 14.5 (May 2018), e1006151.

[14]   Eric A. Bushong, Maryann E. Martone, Ying Z. Jones, and Mark H. Ellisman. "Protoplasmic astrocytes in CA1 stratum radiatum occupy separate anatomical domains". eng. In: *The Journal of Neuroscience: The Official Journal of the Society for Neuroscience* 22.1 (Jan. 2002), pp. 183–192.

[15]   Corrado Cali, Jan Lopatar, Francesco Petrelli, Luca Pucci, and Paola Bezzi. "G-Protein Coupled Receptor-Evoked Glutamate Exocytosis from Astrocytes: Role of Prostaglandins". en. In: *Neural Plasticity* 2014 (Jan. 2014). Publisher: Hindawi, e254574.

[16]   Corrado Calì et al. "A Method for 3D Reconstruction and Virtual Reality Analysis of Glial and Neuronal Cells". In: *JoVE (Journal of Visualized Experiments)* 151 (Sept. 2019), e59444.

[17]   Corrado Calì et al. "Three-dimensional immersive virtual reality for studying cellular compartments in 3D models from EM preparations of neural tissues". en. In: *Journal of Comparative Neurology* 524.1 (Jan. 2016), pp. 23–38.

[18]   Tingting Cui-Wang et al. "Local Zones of Endoplasmic Reticulum Complexity Confine Cargo in Neuronal Dendrites". en. In: *Cell* 148.1 (Jan. 2012), pp. 309–321.

[19]   G. W. De Young and J. Keizer. "A single-pool inositol 1,4,5-trisphosphate-receptor-based model for agonist-stimulated oscillations in Ca2+ concentration." en. In: *Proceedings of the National Academy of Sciences* 89.20 (Oct. 1992), pp. 9895–9899.

[20]   Audrey Denizot, Misa Arizono, U. Valentin Nägerl, Hédi Soula, and Hugues Berry. "Simulation of calcium signaling in fine astrocytic processes: Effect of spatial properties on spontaneous activity". en. In: *PLOS Computational Biology* 15.8 (Aug. 2019), e1006795.

[21]   Audrey Denizot, Misa Arizono, U. Valentin Nägerl, Hédi Soula, and Hugues Berry. "Spontaneous astrocytic calcium traces from organotypic hippocampal slices". en. In: (July 2019). Publisher: figshare Type: dataset.

[22]   Audrey Denizot, Misa Arizono, Valentin Nägerl, Hugues Berry, and Erik De Schutter. "Astrocyte nanoscale morphology controls Ca2+ signals at tripartite synapses". en. In: *bioRxiv* (Feb. 2021). Publisher: Cold Spring Harbor Laboratory Section: New Results, p. 2021.02.24.432635.

[23]   Audrey Denizot, Hugues Berry, and Sharmila Venugopal. "Computational Modeling of Intracellular Ca2+ Signals in Astrocytes." In: *Encyclopedia of Computational Neuroscience* (2019). Submitted, Submitted.

[24]   Audrey Denizot, Hugues Berry, and Sharmila Venugopal. "Intracellular Calcium Signals in Astrocytes, Computational Modeling of". en. In: *Encyclopedia of Computational Neuroscience*. Ed. by Dieter Jaeger and Ranu Jung. New York, NY: Springer, 2020, pp. 1–12.

[25]   Maria Amalia Di Castro et al. "Local Ca2+ detection and modulation of synaptic release by astrocytes". eng. In: *Nature Neuroscience* 14.10 (Oct. 2011), pp. 1276–1284.

[26] Carole Escartin et al. "Reactive astrocyte nomenclature, definitions, and future directions". en. In: *Nature Neuroscience* (Feb. 2021). Publisher: Nature Publishing Group, pp. 1–14.

[27] Rubén Fernández-Busnadiego, Yasunori Saheki, and Pietro De Camilli. "Three-dimensional architecture of extended synaptotagmin-mediated endoplasmic reticulum–plasma membrane contact sites". en. In: *Proceedings of the National Academy of Sciences* 112.16 (Apr. 2015), E2004–E2013.

[28] Joshua B. Foster et al. "Pyridazine-derivatives enhance structural and functional plasticity of tripartite synapse via activation of local translation in astrocytic processes". eng. In: *Neuroscience* (July 2018).

[29] Christel Genoud, Charles Quairiaux, Pascal Steiner, Harald Hirling, Egbert Welker, and Graham W Knott. "Plasticity of Astrocytic Coverage and Glutamate Transporter Expression in Adult Mouse Cortex". en. In: *PLoS Biology* 4.11 (Oct. 2006). Ed. by Charles Stevens, e343.

[30] Leonidas Georgiou, Anaí Echeverría, Achilleas Georgiou, and Bernd Kuhn. "Ca+ activity maps of astrocytes tagged by axoastrocytic AAV transfer". In: *Science Advances* 8.6 (2022). Publisher: American Association for the Advancement of Science, eabe5371.

[31] Daniel T. Gillespie. "Exact stochastic simulation of coupled chemical reactions". In: *The Journal of Physical Chemistry* 81.25 (Dec. 1977), pp. 2340–2361.

[32] László Héja, Zsolt Szabó, Márton Péter, and Julianna Kardos. "Spontaneous Ca2+ Fluctuations Arise in Thin Astrocytic Processes With Real 3D Geometry". English. In: *Frontiers in Cellular Neuroscience* 15 (2021). Publisher: Frontiers.

[33] Janosch P. Heller and Dmitri A. Rusakov. "The Nanoworld of the Tripartite Synapse: Insights from Super-Resolution Microscopy". English. In: *Frontiers in Cellular Neuroscience* 11 (2017).

[34] Christian Henneberger et al. "LTP Induction Boosts Glutamate Spillover by Driving Withdrawal of Perisynaptic Astroglia". en. In: *Neuron* (Sept. 2020).

[35] Iain Hepburn, Robert Cannon, and Erik De Schutter. "Efficient calculation of the quasistatic electrical potential on a tetrahedral mesh and its implementation in STEPS". In: *Frontiers in Computational Neuroscience* 7 (Oct. 2013).

[36] Iain Hepburn, Weiliang Chen, Stefan Wils, and Erik De Schutter. "STEPS: efficient simulation of stochastic reaction–diffusion models in realistic morphologies". en. In: *BMC Systems Biology* 6.1 (2012), p. 36.

[37] Michel K. Herde et al. "Local Efficacy of Glutamate Uptake Decreases with Synapse Size". en. In: *Cell Reports* 32.12 (Sept. 2020), p. 108182.

[38] Yixin Hu, Qingnan Zhou, Xifeng Gao, Alec Jacobson, Denis Zorin, and Daniele Panozzo. "Tetrahedral meshing in the wild". In: *ACM Transactions on Graphics* 37.4 (July 2018), 60:1–60:14.

[39] Jeffrey R. Jones et al. "Mutations in GFAP Disrupt the Distribution and Function of Organelles in Human Astrocytes". In: *Cell Reports* 25.4 (Oct. 2018), 947–958.e4.

[40] Anne Jorstad, Biagio Nigro, Corrado Cali, Marta Wawrzyniak, Pascal Fua, and Graham Knott. "NeuroMorph: A Toolset for the Morphometric Analysis and Visualization of 3D Models Derived from Electron Microscopy Image Stacks". en. In: *Neuroinformatics* 13.1 (Jan. 2015), pp. 83–92.

[41] Conrad M. Kiyoshi et al. "Ultrastructural view of astrocyte-astrocyte and astrocyte-synapse contacts within the hippocampus". en. In: *bioRxiv* (Oct. 2020). Publisher: Cold Spring Harbor Laboratory Section: New Results, p. 2020.10.28.358200.

[42] Natalya Korogod, Carl CH Petersen, and Graham W Knott. "Ultrastructural analysis of adult mouse neocortex comparing aldehyde perfusion with cryo fixation". In: *eLife* 4 (2015), e05793.

[43] Lubomira Lencesova, Andrea O'Neill, Wendy G. Resneck, Robert J. Bloch, and Mordecai P. Blaustein. "Plasma membrane-cytoskeleton-endoplasmic reticulum complexes in neurons and astrocytes". eng. In: *The Journal of Biological Chemistry* 279.4 (Jan. 2004), pp. 2885–2893.

[44] Annamaria Lia et al. "Calcium Signals in Astrocyte Microdomains, a Decade of Great Advances". English. In: *Frontiers in Cellular Neuroscience* 15 (2021). Publisher: Frontiers.

[45] Barbara Lykke Lind, Alexey R. Brazhe, Sanne Barsballe Jessen, Florence C. C. Tan, and Martin J. Lauritzen. "Rapid stimulus-evoked astrocyte Ca2+ elevations and hemodynamic responses in mouse somatosensory cortex in vivo". en. In: *Proceedings of the National Academy of Sciences* (Nov. 2013), p. 201310065.

[46] Irina Lushnikova, Galina Skibo, Dominique Muller, and Irina Nikonenko. "Synaptic potentiation induces increased glial coverage of excitatory synapses in CA1 hippocampus". eng. In: *Hippocampus* 19.8 (Aug. 2009), pp. 753–762.

[47] Tiina Manninen, Riikka Havela, and Marja-Leena Linne. "Computational Models for Calcium-Mediated Astrocyte Functions". In: *Frontiers in Computational Neuroscience* 12 (Apr. 2018).

[48] Julie Marchaland et al. "Fast Subplasma Membrane Ca2+ Transients Control Exo-Endocytosis of Synaptic-Like Microvesicles in Astrocytes". en. In: *Journal of Neuroscience* 28.37 (Sept. 2008), pp. 9122–9132.

[49] Noémie Mazaré et al. "Local Translation in Perisynaptic Astrocytic Processes Is Specific and Changes after Fear Conditioning". en. In: *Cell Reports* 32.8 (Aug. 2020), p. 108076.

[50] Nikolai Medvedev, Victor Popov, Christian Henneberger, Igor Kraev, Dmitri A. Rusakov, and Michael G. Stewart. "Glia selectively approach synapses on thin dendritic spines". en. In: *Phil. Trans. R. Soc. B* 369.1654 (Oct. 2014), p. 20140047.

31

[51] Linnaea E. Ostroff, Mustfa K. Manzur, Christopher K. Cain, and Joseph E. LeDoux. "Synapses lacking astrocyte appear in the amygdala during consolidation of Pavlovian threat conditioning". In: *The Journal of comparative neurology* 522.9 (June 2014), pp. 2152–2163.

[52] Aude Panatier, Misa Arizono, and U. Valentin Nägerl. "Dissecting tripartite synapses with STED microscopy". en. In: *Phil. Trans. R. Soc. B* 369.1654 (Oct. 2014), p. 20130597.

[53] Aude Panatier, Joanne Vallée, Michael Haber, Keith K. Murai, Jean-Claude Lacaille, and Richard Robitaille. "Astrocytes are endogenous regulators of basal transmission at central synapses". eng. In: *Cell* 146.5 (Sept. 2011), pp. 785–798.

[54] Aude Panatier et al. "Glia-Derived d-Serine Controls NMDA Receptor Activity and Synaptic Memory". In: *Cell* 125.4 (May 2006), pp. 775–784.

[55] Ilya Patrushev, Nikolay Gavrilov, Vadim Turlapov, and Alexey Semyanov. "Subcellular location of astrocytic calcium stores favors extrasynaptic neuron-astrocyte communication". eng. In: *Cell Calcium* 54.5 (Nov. 2013), pp. 343–349.

[56] Alberto Perez-Alvarez, Marta Navarrete, Ana Covelo, Eduardo D. Martin, and Alfonso Araque. "Structural and functional plasticity of astrocyte processes and dendritic spine interactions". eng. In: *The Journal of Neuroscience: The Official Journal of the Society for Neuroscience* 34.38 (Sept. 2014), pp. 12738–12744.

[57] Andreas Reichenbach, Amin Derouiche, and Frank Kirchhoff. "Morphology and dynamics of perisynaptic glia". eng. In: *Brain Research Reviews* 63.1-2 (May 2010), pp. 11–25.

[58] Sten Rüdiger and Jianwei Shuai. "Modeling of Stochastic Ca2+ Signals". en. In: *Computational Glioscience*. Ed. by Maurizio De Pittà and Hugues Berry. Springer Series in Computational Neuroscience. Cham: Springer International Publishing, 2019, pp. 91–114.

[59] Dmitri A. Rusakov. "Disentangling calcium-driven astrocyte physiology". en. In: *Nature Reviews Neuroscience* 16.4 (Apr. 2015), pp. 226–233.

[60] Iaroslav Savtchouk and Andrea Volterra. "Gliotransmission: Beyond Black-and-White". en. In: *Journal of Neuroscience* 38.1 (Jan. 2018), pp. 14–25.

[61] Alexey Semyanov, Christian Henneberger, and Amit Agarwal. "Making sense of astrocytic calcium signals — from acquisition to interpretation". en. In: *Nature Reviews Neuroscience* (Sept. 2020). Publisher: Nature Publishing Group, pp. 1–14.

[62] Mark W. Sherwood, Misa Arizono, Aude Panatier, Katsuhiko Mikoshiba, and Stéphane H. R. Oliet. "Astrocytic IP3Rs: Beyond IP3R2". English. In: *Frontiers in Cellular Neuroscience* 0 (2021). Publisher: Frontiers.

[63] Mark William Sherwood et al. "Astrocytic IP3Rs: Contribution to Ca2+ signalling and hippocampal LTP". en. In: *Glia* 65.3 (Mar. 2017), pp. 502–513.

[64] Eiji Shigetomi, Sandip Patel, and Baljit S. Khakh. "Probing the Complexities of Astrocyte Calcium Signaling". eng. In: *Trends in Cell Biology* 26.4 (Apr. 2016), pp. 300–312.

[65] Eiji Shigetomi, Kozo Saito, Fumikazu Sano, and Schuichi Koizumi. "Aberrant Calcium Signals in Reactive Astrocytes: A Key Process in Neurological Disorders". en. In: *International Journal of Molecular Sciences* 20.4 (Jan. 2019), p. 996.

[66] Eiji Shigetomi et al. "Imaging calcium microdomains within entire astrocyte territories and endfeet with GCaMPs expressed using adeno-associated viruses". eng. In: *The Journal of General Physiology* 141.5 (May 2013), pp. 633–647.

[67] Ian F. Smith, Steven M. Wiltgen, Jianwei Shuai, and Ian Parker. "Ca2+ Puffs Originate from Preestablished Stable Clusters of Inositol Trisphosphate Receptors". en. In: *Sci. Signal.* 2.98 (Nov. 2009), ra77–ra77.

[68] Rahul Srinivasan et al. "Ca(2+) signaling in astrocytes from Ip3r2(-/-) mice in brain slices and during startle responses in vivo". eng. In: *Nature Neuroscience* 18.5 (May 2015), pp. 708–717.

[69] Jillian L. Stobart et al. "Cortical Circuit Activity Evokes Rapid Astrocyte Calcium Signals on a Similar Timescale to Neurons". In: *Neuron* 98.4 (May 2018), 726–735.e4.

[70] Min-Yu Sun et al. "Astrocyte calcium microdomains are inhibited by Bafilomycin A1 and cannot be replicated by low-level Schaffer collateral stimulation in situ". In: *Cell Calcium* 55.1 (Jan. 2014), pp. 1–16.

[71] Taufiq-Ur-Rahman, A. Skupin, M. Falcke, and C. W. Taylor. "Clustering of InsP3 receptors by InsP3 retunes their regulation by InsP3 and Ca2+." eng. In: *Nature* 458.7238 (Apr. 2009), pp. 655–659.

[72] Nagendra Babu Thillaiappan, Alap Chavda, Stephen Tovey, David Prole, and Colin Taylor. "Ca2+ signals initiate at immobile IP3 receptors adjacent to ER-plasma membrane junctions". In: *Nature Communications* 8 (Dec. 2017).

[73] Alexei Verkhratsky and Maiken Nedergaard. "Astroglial cradle in the life of the synapse". In: *Philosophical Transactions of the Royal Society B: Biological Sciences* 369.1654 (Oct. 2014).

[74] Alexei Verkhratsky and Maiken Nedergaard. "Physiology of Astroglia". eng. In: *Physiological Reviews* 98.1 (Jan. 2018), pp. 239–389.

[75] Alexei Verkhratsky, Alexey Semyanov, and Robert Zorec. "Physiology of Astroglial Excitability". In: *Function* 1.zqaa016 (Sept. 2020).

[76] Jürgen Wenzel, Grit Lammert, Ursula Meyer, and Manfred Krug. "The influence of long-term potentiation on the spatial relationship between astrocyte processes and potentiated synapses in the dentate gyrus neuropil of rat brain". en. In: *Brain Research* 560.1 (Sept. 1991), pp. 122–131.

[77] Steven M. Wiltgen, Ian F. Smith, and Ian Parker. "Superresolution localization of single functional IP3R channels utilizing Ca2+ flux as a readout". eng. In: *Biophysical Journal* 99.2 (July 2010), pp. 437–446.

[78] Mark R. Witcher, Sergei A. Kirov, and Kristen M. Harris. "Plasticity of perisynaptic astroglia during synaptogenesis in the mature rat hippocampus". eng. In: *Glia* 55.1 (Jan. 2007), pp. 13–23.

[79] Haoxi Wu, Pedro Carvalho, and Gia K. Voeltz. "Here, there, and everywhere: The importance of ER membrane contact sites". en. In: *Science* 361.6401 (Aug. 2018), eaan5835.

[80] Minnie M. Wu, JoAnn Buchanan, Riina M. Luik, and Richard S. Lewis. "Ca2+ store depletion causes STIM1 to accumulate in ER regions closely associated with the plasma membrane". en. In: *J Cell Biol* 174.6 (Sept. 2006), pp. 803–813.

[81] S. Zeller et al. "Modeling of the modulation by buffers of Ca2+ release through clusters of IP3 receptors". eng. In: *Biophysical Journal* 97.4 (Aug. 2009), pp. 992–1002.

Acknowledgements

Author Contributions AD, CC and EDS conceived the research, provided resources and supervised the work. AD and EDS designed the analysis. MFVC and CC curated the electron microscopy data. PP wrote the Blender code for automatic 3D mesh handling. AD did the computational modeling work. AD performed data analysis and visualisation of experimental and computational data. AD wrote the first draft of the manuscript. All authors read and reviewed the manuscript.

Competing Interests Statement The authors declare that they have no competing financial interests.